Invited Review Article: Gas puff imaging diagnostics of edge plasma turbulence in magnetic fusion devices

S. J. Zweben, J. L. Terry, D. P. Stotler, and R. J. Maqueda

Invited Review Article: Gas puff imaging diagnostics of edge plasma turbulence in magnetic fusion devices

S. J. Zweben,[1] J. L. Terry,[2] D. P. Stotler,[1] and R. J. Maqueda[3]

[1]*Princeton Plasma Physics Laboratory, Princeton, New Jersey 08540, USA*
[2]*MIT, Cambridge, Massachusetts 02139, USA*
[3]*X Science LLC, Plainsboro, New Jersey 08536, USA*

Gas puff imaging (GPI) is a diagnostic of plasma turbulence which uses a puff of neutral gas at the plasma edge to increase the local visible light emission for improved space-time resolution of plasma fluctuations. This paper reviews gas puff imaging diagnostics of edge plasma turbulence in magnetic fusion research, with a focus on the instrumentation, diagnostic cross-checks, and interpretation issues. The gas puff imaging hardware, optics, and detectors are described for about 10 GPI systems implemented over the past ~15 years. Comparison of GPI results with other edge turbulence diagnostic results is described, and many common features are observed. Several issues in the interpretation of GPI measurements are discussed, and potential improvements in hardware and modeling are suggested. *Published by AIP Publishing.* [http://dx.doi.org/10.1063/1.4981873]

I. INTRODUCTION

This paper reviews gas puff imaging (GPI) diagnostics of edge plasma turbulence in magnetic fusion research, with a focus on instrumentation, diagnostic cross-checks, and interpretation issues. The gas puff imaging hardware, optics, and detectors are described for the ~10 GPI systems which have been implemented over the past ~15 years. Comparison of GPI results with other edge turbulence diagnostic results is described, and many common features are observed. Several issues in the interpretation of GPI measurements are discussed, and potential improvements in hardware and modeling are suggested. After this section, Sec. II gives a general overview of GPI, Sec. III describes the diagnostic hardware, Sec. IV describes diagnostic cross-checks, Sec. V describes GPI interpretation issues, and Sec. VI is a discussion, including a summary and list of potential improvements.

A. Motivation and background

The motivation for GPI diagnostics is to obtain high resolution data on the space-time structure of the edge turbulence in magnetic fusion devices. The term "edge" in this paper refers to the radial region near the magnetic separatrix (or last closed magnetic flux surface), where the electron temperature is roughly $T_e \sim 10\text{-}100$ eV and where the neutral atoms used in GPI are not completely ionized. The region from the separatrix to the wall is called the scrape-off layer (SOL), and is connected to a wall along a magnetic field line. The edge region just inside the separatrix is hotter and on closed flux surfaces, but GPI can still be used there to the extent that neutrals penetrate (usually within a few centimeters). Both of these edge regions are discussed in this paper.

Edge turbulence is important in determining the particle and energy confinement and the plasma-wall interactions in present toroidal magnetic fusion devices. For example, the high confinement H-mode regime of tokamaks and stellarators is generally associated with a reduction in the edge turbulence just inside the magnetic separatrix, and the width of the scrape-off-layer is at least partially dependent on turbulent transport just outside the magnetic separatrix. These effects will also be important for the successful operation of future magnetic fusion devices such as ITER.

Edge turbulence in magnetic fusion devices has been measured using many diagnostics including Langmuir probes, electromagnetic scattering, visible imaging, and heavy ion beams. The overall result since the 1970s is that the edge plasma turbulence has a high relative fluctuation level (~10%-100%) and has a 3-D structure which is highly elongated along B (the magnetic field direction).[1,2] The causes of edge turbulence have been generically identified as drift-wave and/or interchange instabilities, which are created and sustained by the temperature and/or density gradients in the edge plasma, and the associated radial transport is due the ExB motion driven by electric field fluctuations. However, due to the difficulty of turbulence measurements and the complexity of nonlinear computational simulations, the quantitative connection between experiment and theory is still under investigation, e.g., Ref. 3.

Gas puff imaging uses a puff of neutral gas to increase the local light emission level for improved optical imaging of the space-time structure of the edge plasma turbulence. The gas puff also localizes the region viewed to a nearly 2-D plane within the 3-D structure of the turbulence filaments, i.e., to the plane perpendicular to the local magnetic field direction (see Sec. II A for a description of the GPI geometry). The spatial scales measurable by GPI range from the ion gyro-radius of $\rho_i \sim 0.01\text{-}0.1$ cm up to the radial size scale of the edge region of ~1-10 cm, and the observed frequency range is ~1 kHz to ~1 MHz. Thus edge turbulence as studied with GPI ranges over at least two orders of magnitude in space and time scales, over which there is a broadband spectrum of size-scale and frequency, sometimes accompanied by discrete coherent modes.

B. History of fast imaging in magnetic fusion

The first high speed imaging of plasma fluctuations in magnetic fusion devices was done between 1950s and 1960s using a rotating mirror and streak cameras, e.g., on high-beta plasmas.[4] However, these images showed mainly large-scale MHD instabilities such as kink modes, and not the smaller-scale turbulent structure. Imaging of soft x-rays emitted from the hot plasma core better localized the internal plasma fluctuations, but these results were also dominated by large-scale MHD instabilities such as tearing modes and not the smaller-scale turbulence.

The earliest images of tokamak plasma turbulence were made in the Axially Symmetric Divertor Tokamak Experiment (ASDEX) and Divertor Injection Tokamak Experiment (DITE) tokamaks using high-speed movie film photography.[5–7] Relatively bright field-aligned "filaments" of visible light emission were observed continuously near deuterium or methane gas puff locations at the outer edge of the tokamak. Although these movies did not resolve the filament motion, they did suggest that "the filaments are always present but are normally invisible and are illuminated by the presence of atoms or ions emitting visible radiation."[5]

It was natural to suspect that these visible filaments in the tokamak edge were associated with edge density fluctuations being measured with Langmuir probes and microwaves scattering at that time, and which were theoretically expected to have a filamentary structure.[1,7] This was confirmed using a poloidal array of visible light detectors in the Caltech tokamak, in which the light fluctuations were highly correlated with nearby Langmuir probe measurements of edge density fluctuations.[8] Clear edge filaments were later observed in fast-gated intensified camera images of light emission from the inner bumper limiter (high-field region) of the large tokamak, TFTR.[9] Subsequently, poloidal arrays of deuterium Balmer-α light emission measurements were made in the ASDEX tokamak and the W7-AS stellarator in the vicinity of a gas puffing valve at the outer midplane.[10,11] These Balmer-α fluctuations had similar correlation times, poloidal length scales, and poloidal velocities to the density fluctuations measured using a poloidal array of Langmuir probes near the outer midplane.

Thus by early 2000s it appeared that optical imaging could be used to measure new features of the edge turbulence of magnetic fusion devices, such as the 2-D radial vs. poloidal structure of the turbulent filaments and the motion of coherent "blob" structures in the SOL. This led to the parallel development and first results of gas puff imaging systems on the NSTX[12,13] and Alcator C-Mod tokamaks.[14–17] An overview of GPI is given in Sec. II.

C. Passive turbulence imaging without a gas puff

Before discussing GPI in detail, it is worth noting the advantages and limitations of turbulence imaging without an explicit gas puff. Results of such passive imaging can be quite remarkable and useful, for example, imaging of the Earth's auroral turbulence[18] or the Sun's atmosphere.[19] The obvious limitations of passive imaging are that the source of light is not

under control, and that the fluctuations are integrated along a line-of-sight.

Passive visible imaging of turbulence has been done in linear magnetized plasmas by viewing along the magnetic field, in which the turbulence is assumed to be constant over the parallel scale of the machine. For example, imaging of the unfiltered light emitted by CSDX in an argon plasma showed fluctuating 2-D structures in the radial vs. poloidal plane, which had a statistically significant correlation coefficient ($\sim$0.5) with local density fluctuations measured by a Langmuir probe.[20,21] More recent passive imaging measurements in CSDX used ArI and ArII line filters and identified coherent modes and multiple instabilities during the route to fully developed turbulence,[22,23] and turbulence in linear devices was also imaged with a fast camera in Mirabelle[24] and LAPD.[25]

Fast passive imaging has also been done in the small toroidal device TORPEX using a hydrogen plasma, but without an interference filter.[26] A 4 kHz interchange mode seen by Langmuir probes was also seen in camera images, and the images were tomographically reconstructed to resolve small-scale structures. A gas puff and a camera intensifier were added to improve the system, and a higher cross correlation ($\sim$0.8) was found between the light emission fluctuations and the interchange turbulence in the probe array.[27] Tangential passive imaging of visible light (mainly Hα) was also done in the Q-shu University Experiment with Steady State Spherical Tokamak (QUEST) device in a simple torus configuration, showing blob formation and propagation similar to that in a tokamak SOL.[28]

High speed camera imaging of neutral hydrogen recycling near a limiter was done in the TJ-II stellarator, and the 2-D motion of plasma blobs was observed within the shear layer.[29,30] High speed imaging was also done in the TJ-K stellarator using tangential viewing without filters, but with a small depth of field to minimize the effects due to integration along the line of sight.[31,32] The blob structures seen in the TJ-K camera were similar to those seen by probes.

Passive imaging of edge light emission of Balmer-α light from the midplane SOL has been done in the MAST, in which the separatrix is far from the vessel wall, and the ambient neutral density is high in the SOL.[33,34] The properties of the MAST filaments derived from these passive images are generally similar to those seen using GPI on NSTX (a similar device), and are also well correlated with Langmuir probe signals. Passive imaging results were also obtained from the QUEST, including a detailed analysis of the statistical properties of the edge turbulence.[35] Tangential passive imaging of the filamentary structure of edge localized modes (ELMs) at 150 kHz has recently been reported by the COMPASS (COMPact ASSembly) tokamak.[36]

Finally, fast visible imaging of Balmer-α light was recently done near the X-point and lower divertor regions in MAST[37] and Alcator C-Mod.[38] Clear filaments with complex dynamics were observed near the inner divertor leg, in the private flux zone, and in the SOL outside of the outer divertor leg. Spiral-shaped bands have also been observed in the LiI emission at the divertor plate surface in NSTX, which were highly correlated with midplane GPI images taken

simultaneously and were explained as the field-aligned footprints of SOL blobs.[39]

In summary, passive imaging of turbulence can be useful in linear devices, but is limited in toroidal devices by the line-of-sight integration over the emission sources, which are usually not well localized. Although passive imaging has the advantage of being intrinsically non-perturbative, the 2-D imaging of edge turbulence is more easily done using a controlled gas puff in the GPI configuration, as described below.

II. OVERVIEW OF GPI

A long-term development of the GPI diagnostic was started in parallel on the Alcator C-Mod and NSTX tokamaks.[12–17] Since then, there have been many hardware improvements and successful applications to other magnetic fusion devices, but the basic features of the instrumentation and interpretation of the data remain the same.

This section gives a brief overview of the GPI diagnostic systems in magnetic fusion devices. The basic geometry is described in Sec. II A, some examples of GPI turbulence images are in Sec. II B, and a summary of what GPI can measure is in Sec. II C. The choice of the GPI gas is discussed in Sec. II D, the GPI spatial resolution is discussed in Sec. II E, and the interpretation of GPI signals is discussed in Sec. II F. Further details on each of these topics are given in Secs. III–V.

A. GPI geometry

The basic idea behind gas puff imaging is illustrated in Fig. 1(a). At the left is a highly idealized picture of a single 3-D plasma edge turbulence filament, which is aligned along B, the magnetic field direction. Also shown schematically is a neutral gas puff cloud intersecting this filament within a small length along the filament. If the neutral atom light emission from the filament increases significantly within this gas cloud, then the 2-D radial vs. poloidal structure of the filament in the plane perpendicular to B should be visible when viewed from along the local B direction (labeled "GPI view"). Ideally, the gas cloud should be a narrow "sheet beam" perpendicular to the magnetic field in order to optimize the spatial resolution of the magnetic field-aligned structures as seen in GPI.

The 2-D cross section of the filament perpendicular to B is the circular region labeled "blob" in this generic figure. Although the term "blob" is generally used to mean the 2-D cross section of relatively isolated density filaments in the SOL of tokamaks, similar magnetic-field-aligned plasma fluctuations of variable amplitude exist both inside and outside the magnetic separatrix in tokamaks and other toroidal devices. The determination of the structure and motion of these edge plasma fluctuations is the goal of GPI.

A more specific illustration of the GPI geometry is shown in Fig. 1(b). The structures in yellow are edge density fluctuations aligned along the magnetic field near the separatrix, as taken from the turbulence simulation code XGC-1 run for DIII-D.[40,41] The gray is the GPI gas cloud shape from DEGAS 2, and the yellow glow is where the filaments intersect the
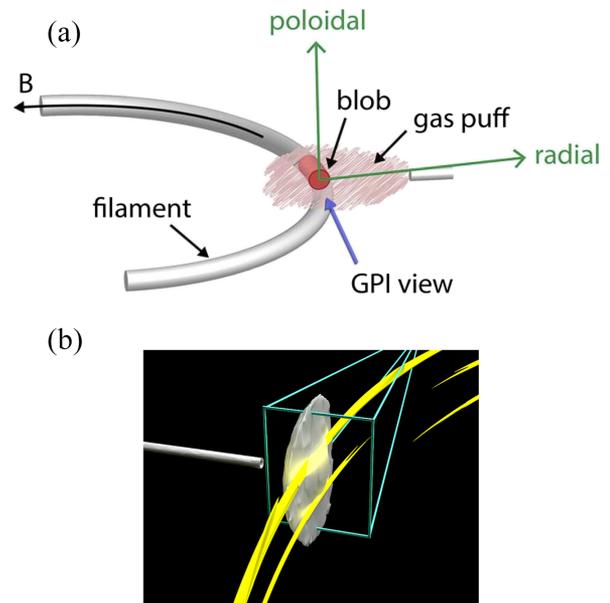

FIG. 1. Gas puff imaging (GPI) geometry in a tokamak. The simplified picture in (a) shows a single 3-D plasma edge filament aligned along the magnetic field direction B, along with a schematic illustration of a gas puff cloud. [Reproduced with permission from Fig. 1 of Cao *et al.*, Fusion Sci. Technol. **64**, 29 (2013). Copyright 2013 American Nuclear Society.] When viewed along the local B field direction in the cloud, the 2-D structure of the filament perpendicular to B should be fairly clearly visible (i.e., the "blob"). The more realistic image in (b) was constructed using plasma turbulence simulation outputs of XGC-1 and gas cloud outputs from DEGAS 2 [visualization provided by D. Pugmire, private communication (2016).[169] The yellow filaments are edge density structures near the separatrix in the XGC-1 output, which are aligned along the magnetic field. The gray is the GPI gas cloud shape from DEGAS 2, and the yellow glow is where the filaments intersect the computed gas cloud. The blue box is the simulated GPI camera view, and the tube at the left is the GPI gas puffer.

computed gas cloud. In this case, the radial width of the GPI gas cloud is smaller than its poloidal or toroidal width. Other examples of GPI usage are mentioned in Sec. II C.

Thus GPI measures the 2-D structure of edge plasma turbulence by localizing the measurement using a gas puff, and by interpreting the neutral line emission from that puff assuming that the turbulence is aligned parallel to B. The assumption of a long parallel structure is firmly based on the theoretical idea of rapid motion of electrons along B, and confirmed by measurements showing a high correlation of density fluctuations parallel to B. This GPI "cross-beam" imaging technique is generically similar to other plasma diagnostic methods such as beam emission spectroscopy (BES)[42] and planar laser induced flourescence (LIF).[43] Obviously an important requirement for the GPI diagnostic is that the gas puff does not significantly perturb the local plasma or the edge turbulence itself (see Sec. V F).

B. Examples of GPI images

Some examples of GPI edge turbulence images from four tokamaks are shown in Figs. 2–5. Each of these figures also shows a different method of presenting the data, as described below.

Figure 2 shows GPI images from the NSTX tokamak made over a 24 cm (radial) × 24 cm (poloidal) region near the outer midplane using a D_2 gas puff and a Balmer-α filter, with a
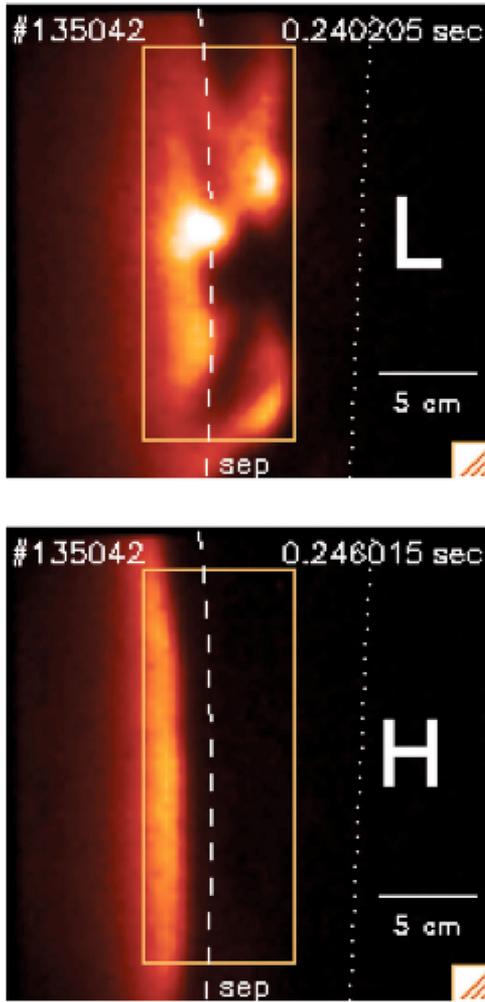
FIG. 2. GPI images from the NSTX tokamak made near the outer midplane over a 24 cm × 24 cm region using a D_2 gas with a Balmer-α filter and a 2.1 μs camera exposure time. [Reproduced with permission from Phys. Plasmas **17**, 102502 (2010). Copyright 2010 AIP Publishing LLC.] At the top is a typical L-mode plasma, and at the bottom is a quiescent H-mode plasma later in the same shot. In both cases the *raw camera data* are displayed using the same false linear color scale (white as maximum and black as zero), with the poloidal direction vertical, the radial direction horizontal (outward to the right), and the magnetic separatrix from the EFIT reconstruction is shown by the dashed line. The data are analyzed only within the orange boxes since Dα emission is too small in the low electron temperatures near the wall (right of the box), and also too low farther inside the plasma where the ionization occurs at high temperatures (left of the box).

2.1 μs camera exposure time.[44] At the top is an example of a typical L-mode image showing the complex turbulence structure, and at the bottom is an H-mode image later in the same shot, which is nearly quiescent (turbulence-free). In both cases the *raw camera data* are displayed using the same false linear color scale (white as maximum and black as zero), with the poloidal direction vertical, the radial direction horizontal (outward to the right), and the magnetic separatrix shown by the dashed line. These data were analyzed in detail only within the orange boxes, since Dα emission was too small in the low electron temperature region near the wall (right of the box), and also too small farther into the hot plasma where the deuterium was largely ionized (left of the box). Thus GPI measures the turbulence within the radial "window" where the maximum Balmer-α emission from the deuterium puff occurs.

Figure 3 shows GPI images from the Alcator C-Mod tokamak from two different 6 cm × 6 cm regions taken after puffing D_2 gas with a Balmer-α line filter.[45] The lower image is from a GPI view of the region outboard and somewhat above the lower X-point, while the upper image is from a GPI view of the outer midplane region. Both were taken in H-mode plasmas. In this instance the images are normalized with respect to the time-averaged images to show the structure of the *relative fluctuation level in a selected image*, where white is 1.5 or greater and black is <0.5, and the low signal region far inside the separatrix is forced black. The fluctuation levels are often large in both locations (greater than ±50%). Note the blob-like structure in the midplane image, while the structures outboard of the X-point are elongated and significantly tilted with respect to the local separatrix. The elongations and tilts in the lower part of the X-point-region image are thought to be due to magnetic mapping of outboard near-midplane blobs, while those in the upper part of the image are thought to be the result of a toroidal extent to the gas puff and the filament extension along B (Ref. 45).

Figure 4 shows a time sequence of GPI images from the TEXTOR tokamak made at the outer midplane using deuterium gas with a Balmer-α filter. Each of these frames covers a 12 cm × 12 cm region and has a camera exposure time of 6 μs.[46] These images have their time average image *subtracted* to show more clearly the positive (red) and negative (blue) excursions from the mean signal. The poloidal motion of one positive structure is shown by the black dashed line, and the last closed flux surface is shown by the green dashed line, with the radially outward direction toward the left. These data are from an Ohmic discharge.

Figure 5 shows a time sequence of GPI images from the ASDEX Upgrade tokamak created using a 2-D conditional averaging (CA) technique based on the normalized light intensity fluctuations.[47] The GPI data were taken again with a deuterium gas puff and Balmer-α filter, here with 8 μs between frames during an inter-ELM period in an H-mode plasma, and over a region of ~5 cm × 5 cm just below the outer midplane. The reference pixel is the small "x," the threshold for CA is two times the standard deviation, and 556 trigger events were averaged to produce these averaged images. The positive blob structure shown (red) was born inside the separatrix (dashed line), and on average propagated radially outward (to the right) and poloidally in the ion diamagnetic drift direction (i.e., downward) over ~50 μs. The fluctuation amplitude is scaled to a maximum at t = 0, and a faint negative (hole) structure is also shown in blue.

C. What does GPI measure?

A list of measurements which have been done using GPI is given in Table I. The GPI diagnostic is most often used to measure edge turbulence by analyzing the space vs. time patterns of GPI light emission, such as those in Figs. 2–5. For example, the turbulence correlation lengths can be obtained from cross correlations of the GPI light emission vs. poloidal or radial position, and turbulence velocities can be obtained from time-delayed spatial cross correlations or Fourier mode analyses. The raw data are often normalized by the
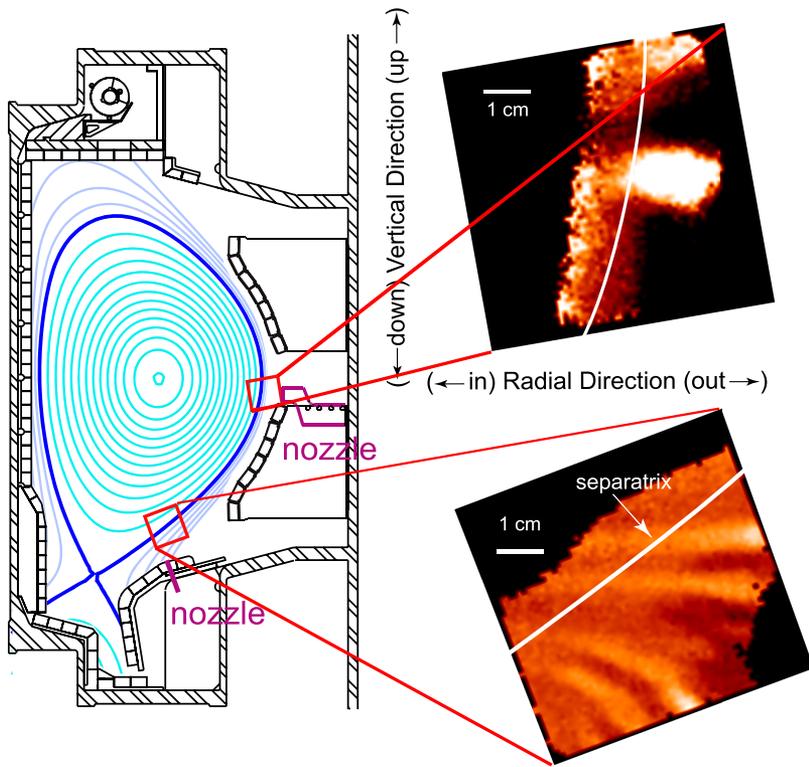
FIG. 3. GPI images from the Alcator C-Mod tokamak made at two different 6 cm × 6 cm regions using D_2 gas with the Balmer-α line filter. The imaged regions are shown schematically along with the plasma equilibrium at the time when the image from outboard of the lower X-point was taken.[45] The other imaged region is at the low-field-side midplane. The four-hole nozzle at the LFS midplane and the single-hole nozzle in the outer divertor target, below the lower imaged region, are also shown. These images are normalized with respect to the time-averaged images of each region to show the structure of the *relative fluctuation levels*, where white is 1.5 and black is 0.5, and the low signal region well inside the separatrix is forced black. The maximum fluctuation levels are large (±50%) in both locations, and the structures in the X-point region are significantly tilted with respect to the local separatrix. Both discharges are in H-mode.
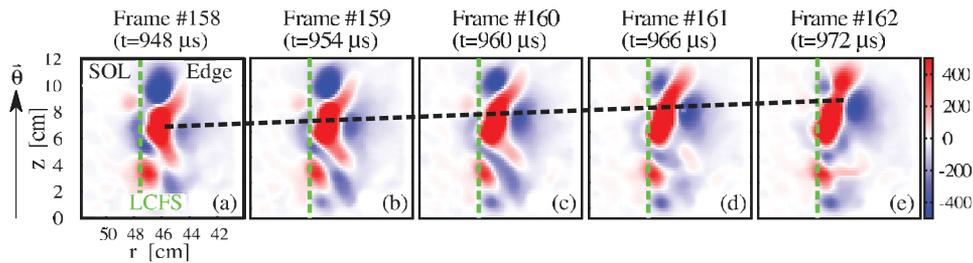

FIG. 4. A time sequence of GPI images from the TEXTOR tokamak made with camera exposure times of 6 μs each over a 12 cm × 12 cm region at the outer midplane using D_2 gas with a Dα filter. [Reproduced with permission from Rev. Sci. Instrum. **84**, 053510 (2013). Copyright 2013 AIP Publishing LLC.] These images have their time averages image *subtracted* to show more clearly the positive (red) and negative (blue) excursions from the mean signal. The poloidal motion of one positive structure is shown by the black dashed line, and the last closed flux surface is shown by the green dashed line, with the radially outward direction toward the left. These data are from an Ohmic discharge.
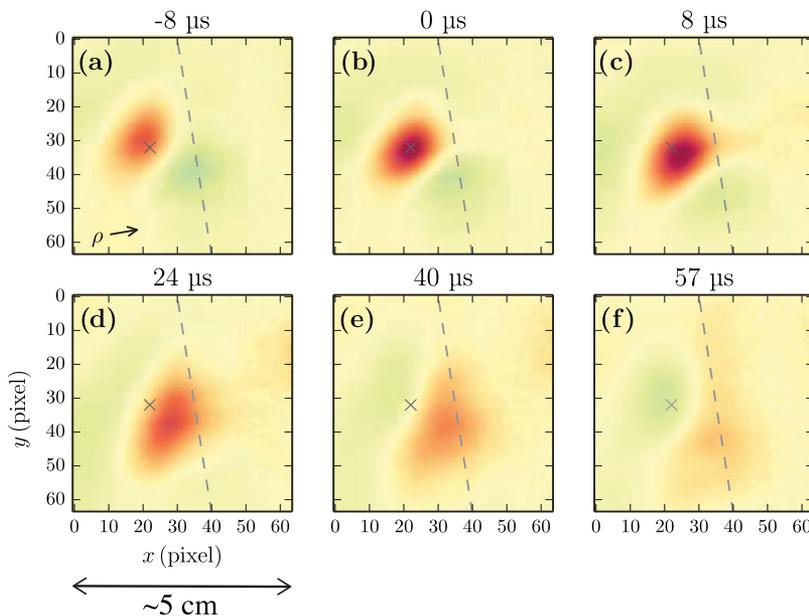

FIG. 5. A time sequence of GPI images from the ASDEX Upgrade tokamak created using a 2-D conditional averaging (CA) technique based on the normalized light intensity fluctuations. [Reproduced with permission from Fig. 4 of Fuchert *et al.*, Plasma Phys. Controlled Fusion **56**, 125001 (2014). Copyright 2014 IOP Publishing.] The GPI data were taken with a deuterium gas puff and Dα filter with 8 μs between frames during an inter-ELM period in an H-mode plasma, and over a region of ~5 cm × 5 cm just below the outer midplane. The reference pixel is the small cross, the threshold for CA is two times the standard deviation, and 556 trigger events were averaged to produce these averaged images. The positive blob structure shown (red) was born inside the separatrix (dashed line), and on average propagated radially outward (to the right) and poloidally downward over ~50 μs. The fluctuation amplitude is scaled to a maximum at t = 0, and a faint negative (hole) structure is also shown in blue.

TABLE I. Measurements done with GPI.

Measurement	Typical values
Relative fluctuation level	~5%-100%
Frequency spectrum	~1-1000 kHz
Autocorrelation time	~1-100 μs
Radial correlation length	~0.5-5 cm
Poloidal correlation length	~1-10 cm
Parallel correlation length	~1-10 m
Poloidal turbulence velocity	~0-10 km/s
Radial turbulence velocity	~0-3 km/s
Zonal flow oscillations	~2-20 kHz
Quasi-coherent edge modes	~2-200 kHz
Blob generation rate	Highly variable
Blob structure and motion	Highly variable
Edge localized modes (ELMs)	Highly variable

time-averaged image before analysis (as in Fig. 3), in order to remove time-independent spatial variations due to the cloud emissivity shape, which are of order unity in the raw image (as in Fig. 2).

It is important to stress that GPI measures the visible light emitted by neutral atom line radiation from the gas puff and does not directly measure the electron density or temperature fluctuations. However, it is sometimes assumed that the line emission fluctuations are dominated by electron density fluctuations, which are known to be large in the edge and which have properties very similar to the visible light fluctuations measured by GPI. This interpretation is discussed in detail in Secs. II F and V B.

The space-time range of GPI turbulence measurements is defined by the region over which the visible neutral line emission has a high signal/noise and signal/background ratio, which is typically within ~0.5-5 cm and ~1-100 μs (see Table I). This measurement range corresponds to regions where the electron temperature is above $T_e \sim 5$ eV where the excitation rate of the neutral lines becomes significant, and below $T_e \sim 200$ eV, above which the neutrals are largely ionized (see Sec. II F). This sensitivity to the atomic physics defines the radial range over which the GPI can make measurements and is usually located within a few centimeters inside and outside the magnetic separatrix in present magnetic fusion devices. This is a region where the edge turbulence is normally strong and the radial transport due to the turbulence is large. In large fusion devices such as ITER, the neutrals from a gas puff may not penetrate inside the separatrix, so GPI would then be useful only in the SOL.

A popular use of GPI is to measure the 2-D structure and motion of discrete plasma "blobs" or "filaments," which form near the magnetic separatrix and move outward into the scrape-off layer (SOL). These structures are highly variable and not well understood, despite much theoretical and experimental analyses.[48,49] The 2-D blob formation and motion into the SOL can be measured by GPI in present devices, and the 2-D motion of the turbulence can be evaluated by various velocimetry methods, as discussed in Sec. V G. For a full interpretation of the GPI observations of blobs, it is also useful to have plasma potential and electric field fluctuation measurements, for example, from Langmuir probes.

GPI has also been used to measure the quasi-coherent edge oscillations[50–52] and edge localized modes (ELMs).[53,54] The GPI light signal will respond to any density/temperature perturbations associated with edge instabilities and also indirectly to any radial movement of edge magnetic flux surfaces which causes local density/temperature perturbations.

Studies of nonlinear interactions between the two fluctuation fields (density and velocity) have been performed using GPI, where velocimetry of GPI images has been used to infer the turbulent velocity field. This has allowed evaluations of the coupling between Geodesic Acoustic Modes (GAM), zonal flows (ZF), and quasi-coherent edge modes,[55] as well as the turbulent kinetic energy transfer between zonal flows and the ambient small scale edge turbulence.[56] These studies of the turbulence dynamics are then used to examine the underlying physics of confinement-mode transitions, e.g., L-mode to H-mode transitions and I-mode to H-mode transitions.[57]

D. Choice of GPI gas and spectral line

The neutral gas used for GPI has usually been either deuterium or helium since these have the lowest atomic number and are generally the least perturbing to the plasma. Since most fusion experiments use deuterium as the main fueling gas, deuterium puffing is sometimes preferable to keep the radiation losses low and can usually be done without significantly increasing the average plasma density, for example, in NSTX.[58] Helium GPI can be used to provide a greater signal-to-background contrast ratio, especially where the background Balmer-α light level is high, e.g., at high plasma density or near sources of edge recycling (e.g., in Alcator C-Mod or RFX-Mod). Helium may also produce a more localized GPI gas puff since a deuterium puff can create high energy neutrals through molecular dissociation and charge exchange. Other gases such as methane or neon might be used as a source of neutral atoms, but these higher Z gases radiate more and tend to perturb the edge plasma.

It is highly desirable to use a single neutral atom spectral line for GPI, rather than the total visible light emission, in order to have a clear relationship between the line emission rate and the local density and temperature fluctuations (see Sec. II F). The usual spectral lines for GPI are Balmer-α at 656.3 nm for deuterium and the 587.6 nm or 667.8 nm lines for helium since these are the brightest visible lines. In edge fusion plasmas, the Balmer-α and HeI 587.6 nm lines have roughly similar brightness for the same puff rate. Line intensity ratios can also be used to measure the edge density and temperature fluctuations as in the thermal helium beam (THB) diagnostic,[59] and measurements have been made of 2-D edge profiles (not turbulence) using this technique.[60] Ion emission lines, such as from HeII, will tend to form an elongated plume along the magnetic field direction, and so would provide a less localized GPI measurement (depending on the species and plasma parameters).[61]

E. GPI spatial resolution

If the GPI gas cloud line emission is very strong compared with the background plasma emission, and if the GPI

gas cloud were confined entirely within a 2-D plane perpendicular to B, then the spatial resolution of the GPI would not be limited by the local magnetic field line tilt angle or curvature. At the other extreme, without any GPI gas puff, the full 3-D filamentary structure of the background plasma emission would be seen, and it would be difficult to unfold the 2-D structure perpendicular to B. In between these limits, the spatial resolution of the GPI will depend on the viewing geometry, toroidal extent of the gas cloud, and the local magnetic field line geometry.

For optimum GPI spatial resolution, the GPI sightline axis should be aligned as closely as possible at the plasma magnetic field line pitch angle within the GPI cloud, as illustrated in Fig. 1(a). However, since the GPI sightline direction varies within a given field of view, and since the plasma magnetic field direction often varies from one shot to another, there is generally a small angle between the GPI sightline and the local B field direction. Focusing on tokamak geometry, if the angle between a GPI sightline and the local B field line is θ_B, the image of a narrow field-aligned filament will be spread along the angle of the misalignment direction (either radial or poloidal) by

$$\Delta x \sim L_{\parallel,\text{cloud}} \tan \theta_B, \tag{1}$$

where $L_{\parallel,\text{cloud}}$ is the approximate length of the GPI gas cloud along the B field line. This assumes that the filament emission is constant along B within the GPI gas cloud, that $L_{\parallel,\text{cloud}} << R$ (major radius), and that the optical depth of the line emission is much longer than $L_{\parallel,\text{cloud}}$. For example, if $L_{\parallel,\text{cloud}} \sim 10$ cm (as might be produced from a gas nozzle located ~10 cm from the central GPI viewing chord) and the misalignment angle is $\theta_B \sim 6°$ (as found at the edge of a typical optical system), this limiting resolution would be $\Delta x \sim 1$ cm. This spatial resolution Δx will affect the measured turbulence size scale if Δx is comparable to or larger than the turbulence correlation length in that direction.

The poloidal angle of the edge B field line can sometimes be adjusted to match the GPI sightline by varying the ratio of the plasma current to the toroidal field. In that case, there will be no significant degradation in the poloidal turbulence resolution, at least at that aligned point in the GPI image. However, the minimum radial resolution (i.e., perpendicular to the poloidal direction and to B) will depend on the toroidal field line *curvature* within the plane of the B field line, i.e., by the radial length Δx_{rad} of the toroidal arc segment within the cloud,

$$\Delta x_{\text{rad}} \sim (L_{\parallel}, \text{cloud})^2/8R. \tag{2}$$

For example, if $L_{\parallel,\text{cloud}} = 10$ cm and $R = 100$ cm, $\Delta x_{\text{rad}} \sim 0.1$ cm. For most cases, this limiting resolution is much smaller than that of the angular misalignment effect in Eq. (1).

For example, in NSTX the distance from the GPI camera lens to the GPI gas cloud is ~70 cm, so even when the GPI optical axis is perfectly aligned with the local magnetic field at the center of the GPI image, the misalignment angle is $\theta_B \sim 8°$ at a distance of 10 cm poloidally from this center, which is still within the 2-D typical imaging region (see Fig. 2). This degree of misalignment will cause a spatial smearing of ~1-2 cm for a calculated gas cloud length of $L_{\parallel,\text{cloud}} \sim 12$ cm, which is rel-

atively small compared with the typical turbulence correlation length of ~5 cm in NSTX. However at the edge of the optimally aligned images in NSTX, or in shots where the edge field lines are not well aligned with the GPI optical axis, this angle can be up to $\theta_B \sim 20°$, at which point the loss of resolution can affect the shape of the 2-D correlation function, as discussed in detail elsewhere.[62] The range of misalignment also depends on the edge magnetic shear, which is relatively large in NSTX.

In general, the exact geometrical resolution of a GPI system can be determined from a 3-D simulation (or measurement) of the GPI gas cloud, the B field line geometry, and the viewing geometry. Other factors which can affect the spatial resolution are the optical resolution and the camera pixel resolution; these can be combined into a single 2-D resolution function describing the total diagnostic spatial resolution as a function of the position within the GPI image.

F. Interpretation of GPI measurements

Gas puff imaging measures the neutral atom line emission from a localized deuterium or helium gas puff at the edge of a magnetic fusion plasma. However, the objective of GPI is to visualize the edge plasma turbulence, which consists of plasma density and temperature fluctuations. An understanding of the relationship between the measured visible light fluctuations and the underlying plasma fluctuations is thus required to establish this connection.

The intensity of the line emission from neutral atoms in a plasma can be most simply expressed as

$$I = n_o f(n_e, T_e), \tag{3}$$

where n_o is the local neutral atom density, n_e and T_e are the local electron density and temperature, and the function f is the ratio of the density of the upper level of the radiative transition to the ground state density times the rate of decay of the upper level. For example, for the deuterium Balmer-α transition, n_0 is the density of the 1s ground state, $n_0 = n_D(1s)$ and

$$f(n_e, T_e) = \left[\frac{n_D(n=3)}{n_D(1s)} \right] A_{3 \to 2}, \tag{4}$$

where $A_{3 \to 2} = 4.41 \times 10^7$ s^{-1} is the radiative decay rate (Einstein coefficient) for the transition.

To determine the quantity in brackets here, one needs to establish the population distribution of the excited states. Their time evolution can be written as a balance between radiative decay, electron collisional excitation, de-excitation, and ionization. The time scales for the excited state decay and electron collisional processes are much shorter than those of neutral transport. To a good approximation, then, one can set the time derivative in the excited state rate balance equations to zero and solve the resulting set of equations for the excited state densities relative to that of the ground state; this is the collisional radiative approximation.[63] This yields the "population coefficients," such as the one in Eq. (4), as functions of T_e, through the temperature dependence of the collisional rate coefficients, and n_e, via its appearance in each of the rate balance equations.[64–66] The use of Eq. (3) in interpreting GPI

data also assumes that changes in the plasma density and/or temperature are instantly reflected in the rate of light emission, that only the electron impact causes the excitation, and that the photons produced travel unimpeded to the detector. The validity of these assumptions is discussed in Secs. V C and V D.

Figures 6(a) and 6(b) show $f(n_e, T_e)/n_e$ for the 656.3 nm deuterium line and 587.6 nm helium line used most often for GPI. The former represent the output of a collisional radiative model derived from the one described in Ref. 67, with cross sections from Ref. 68 and newer cross sections for excitation from the ground state to n = 3, 4, and 5 from Refs. 69 and 70. As with the deuterium electron impact ionization rate, the photon emission rate increases rapidly with temperature below about 10 eV and then peaks at roughly 100 eV. The near overlap of the $n_e = 10^{11}$ and 10^{12} cm^{-3} curves implies that $f(n_e, T_e)$ is nearly linear in n_e at those densities; however, at higher densities, collisional excitation and de-excitation compete with radiative decay in depopulating the n = 3 excited state. Balmer-α photons can also be generated during dissociation of D_2 and D_2^+. The effective rate for this process is shown in Fig. 6(a) and will be discussed in more detail in Sec. V D.
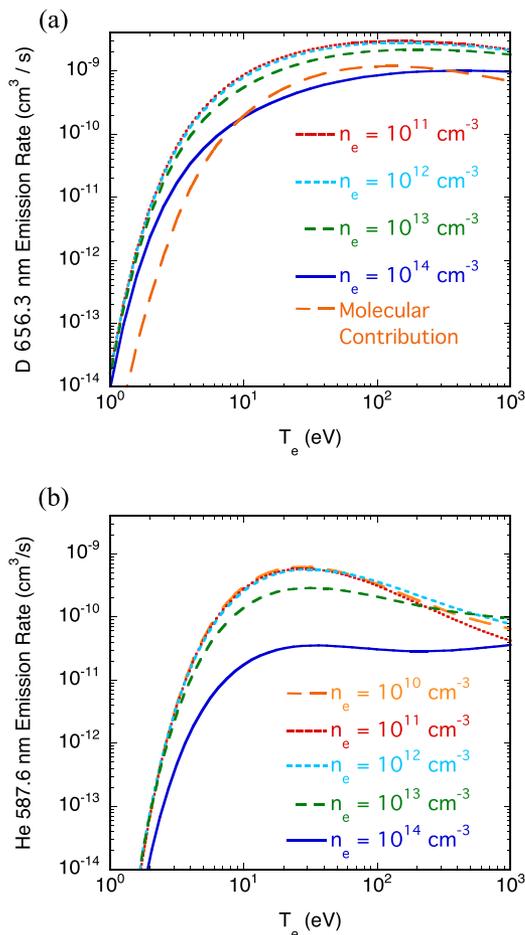
The helium data were produced by the code documented in Ref. 71, which was in turn based on the work by Fujimoto.[72] Again, the temperature variation is strong below 10 eV, albeit with a rate lower than that in Fig. 6(a) because of the greater energy required to excite the atom to the upper state of the transition. The presence of the second electron in the system results in a much more complex behavior at higher densities.

To help determine the sensitivity of the line emission to density and temperature fluctuations at a given point in

FIG. 6. (a) Deuterium Balmer-α (656.3 nm) and (b) HeI 587.6 nm photon emission rate per electron per neutral atom, i.e., $f(n_e, T_e)/n_e$ in Eq. (3) obtained from the collisional radiative model described in the text. The photon emission rate per electron per deuterium molecule is included in (a) for comparison; these contributions are described in Sec. V C.
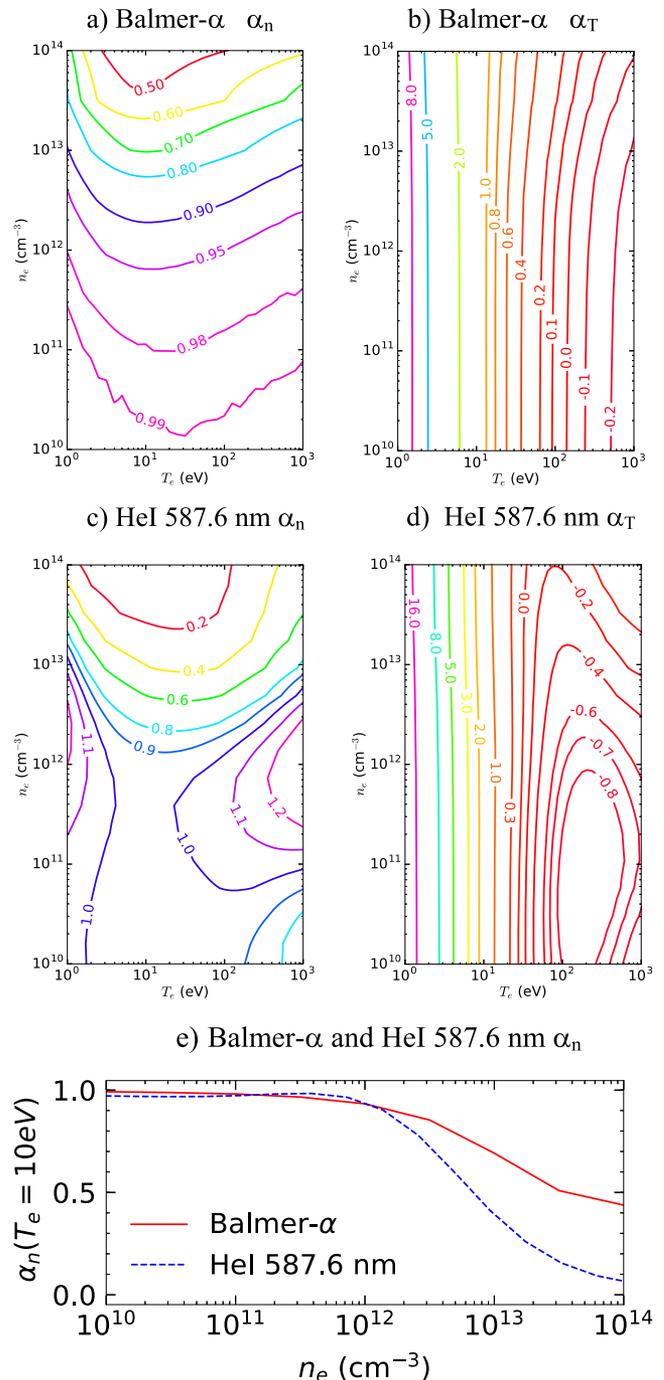
FIG. 7. (a) Density and (b) temperature exponents α_n and α_T as defined in Eq. (5) for the deuterium Balmer-α (656.3 nm) data shown in Fig. 6(a). (c) and (d) are the analogous quantities for HeI (587.6 nm). (e) Density exponent variation with respect to n_e at $T_e = 10$ eV.

parameter space, we define

$$\alpha_n = \frac{\partial \ln f}{\partial \ln n_e} \text{ and } \alpha_T = \frac{\partial \ln f}{\partial \ln T_e} \tag{5}$$

and refer to α_n and α_T as the local density and temperature "exponents," that is,

$$f \propto n_e{}^{\alpha_n} T_e{}^{\alpha_T}. \tag{6}$$

The values of these exponents computed from Figs. 6(a) and 6(b) are shown in Figs. 7(a)–7(d). At relatively low densities ($n_e \leq 10^{13}$ cm^{-3} for D, $n_e \leq 10^{12}$ cm^{-3} for He), the line emission is nearly proportional to density independent of temperature, i.e., $\alpha_n \sim 1$; at higher densities collisional processes reduce the density exponents to less than one. This is demonstrated explicitly at $T_e = 10$ eV in Fig. 7(e). The electron temperature exponents are nearly independent of density below $n_e \leq 10^{14}$ cm^{-3}, and α_T decreases monotonically between $T_e \sim 1$ eV and 100 eV.

Thus the response of GPI to local plasma fluctuations depends on both the electron density and temperature fluctuations, which are not normally measured on the space-time scales of the edge turbulence (otherwise GPI would not be needed). The interpretation of GPI is also complicated by the possibility that the local neutral density is itself affected by the fluctuations, e.g., due to depletion by ionization or non-local effects. These issues are discussed in further detail in Secs. V B and V E.

III. GPI DIAGNOSTIC HARDWARE

This section describes the GPI diagnostic hardware used on the devices listed in Table II. Most of these are tokamaks or stellarators, two are reversed field pinches (RFPs), one is a magnetic mirror device, and one is a simple toroidal device (TORPEX). We first discuss the generic features of the gas puff hardware in Sec. III A, the optics in Sec. III B, the detectors in Sec. III C, and the calibrations in Sec. III D. Special features for each system are noted in Sec. III E.

A. Gas puff

The GPI gas is puffed into the plasma edge, which has a typical ambient neutral pressure of $<10^{-6}$ bar, although the

TABLE II. GPI diagnostic systems.

Machine	Type	GPI views	GPI gas	GPI detectors
Alcator C-Mod	Tokamak	4	D,He	Phantom, APD
ASDEX	Tokamak	1	D	PM
ASDEX-U	Tokamak	1	D	Phantom
EAST	Tokamak	2	He	Phantom
Gamma 10	Mirror	1	H	Photron
Heliotron J	Stellarator	1	D	Photron
NSTX	ST	1	D,He	Phantom, PM
RFX-mod	RFP	3	He	PM
TJ-II	Stellarator	1	H,He	Photron, PSI-5
TEXTOR	Tokamak	1	D	PSI-5
TORPEX	Toroidal	2	He	Photron
TPE-RX	RFP	3	D	PM

actual neutral density in the SOL is quite variable and difficult to measure. The GPI gas puff should be large enough to increase the local neutral density significantly (e.g., by ×5-10), such that the light emission within the puff volume is bright enough to be measured on a turbulence (few μs) time scale. The species, flow rate, and duration of the gas puff are chosen to produce a good GPI signal while minimally perturbing the plasma edge or the edge turbulence.

The simplest GPI gas puffer consists of a neutral gas reservoir, a fast gas valve, and a gas nozzle mounted on the wall inside the vacuum vessel. The gas in the reservoir is at room temperature, and the pressure is adjustable up to ~1-2 bars. The valve is typically a piezoelectric which can open or close in ≤ 10 ms, and the nozzle can be as simple as a circular hole with ~1 mm diameter. The same gas puff hardware can be used for either deuterium molecules or helium atoms.

The GPI gas puff rate will be roughly $\Phi_{gas} \sim n_{man} v_{th} A_{hole}$, where n_{man} is the manifold gas density (which can be much less than the reservoir density for short pulses), v_{th} is the atom speed (which can be higher than room temperature inside the plasma), and A_{hole} is the nozzle hole area. To get a rough estimate of the GPI gas density, we assume that the manifold has helium at 0.1 bar, i.e., $n_{man} \sim 3 \times 10^{18}$ atoms/cm^3 with $v_{th} \sim 10^5$ cm/s (room temperature) and $A_{hole} \sim 10^{-2}$ cm^2, in which case the gas puff rate is $\Phi_{gas} \sim 3 \times 10^{21}$ atoms/s. If this gas expands freely into the chamber without heating, the average gas density would be $n_o \sim 5 \times 10^{13}$ atoms/cm^3 at ~10 cm from the hole. The actual gas influx rate and its density in the plasma will depend on the chosen manifold pressure and the temperature of the neutrals in the plasma. For example, at the relatively high peak gas puff rate of ~6.6 × 10^{21} deuterium atoms/s in NSTX,[58] the estimated maximum neutral atom density in the GPI cloud is $n_o \sim 5 \times 10^{12}$ cm^{-3} (see Sec. V D), which is ~10 times higher than the local background neutral density as calculated with DEGAS 2.[73]

GPI gas nozzles most often consist of many small holes designed to fill the GPI optical field of view in each experiment. For example, NSTX has used a line of thirty ~1 mm diameter holes spaced 1 cm apart on a ~1 cm diameter tube aligned poloidally near the outer midplane.[13,58] TEXTOR has used a nozzle of 100 holes of 0.5 mm diameter and 15 mm length drilled into a 2 cm × 6 cm rectangular matrix.[46] Alcator C-Mod has used a 1 mm diameter capillary tube to bring the GPI gas to a four-hole nozzle near the outer midplane, and single-hole nozzles at the inner wall and outer divertor target.[45]

The angular distribution of gas emitted from these nozzles depends on the gas flow regime (Knudsen number) and the shape and distribution of the holes. The smaller the angular spread of the gas along B, the better the spatial resolution of the GPI system (see Sec. II E). Thermal gas flow through a plane hole can be characterized by a cosine to a power distribution, with an exponent of 1 most commonly used. Laboratory measurements of viscous gas flow through a capillary yielded an exponent of 5/2.[74] The TEXTOR GPI nozzle is operated in a narrow divergence flow regime with holes of an aspect ratio 30:1, which produces a low angular divergence measured to be ~20° FWHM, i.e., much narrower than the ~120° FWHM

expected for a cosine distribution.[46] The spatial uniformity of the GPI gas cloud is also important, and is discussed in Sec. V A.

The minimum GPI gas pulse duration is ~10 ms due to the valve opening and gas transit time from the valve to the nozzle, which is long compared to the ~10 μs turbulence time scale. Many GPI systems operate with single short gas puff to maximize the signal level for a given gas influx during a plasma shot, but some systems are operated continuously at a lower reservoir pressure and lower puff rate over longer times (e.g., ~0.5 s in TEXTOR).

B. Optics

The optics in GPI systems is designed to form an image of the GPI gas cloud on a fast camera or a set of discrete light detectors. The details of the optical designs are different for each experimental device, so only the general optical issues are reviewed in this section. References to figures of the optical layouts for various specific machines are cited in Sec. III E.

The optical view of the GPI gas puff should be aligned as closely as possible with the edge magnetic field lines, which are generally parallel to the vessel wall. The first optical element in a GPI system is normally a mirror mounted just inside the vessel wall, which deflects the gas cloud image into a small telescope lens, which then transmits the image to the detector through a set of relay lenses and/or a coherent fiber bundle. The image must also be transferred across a vacuum boundary to the detector in air. The vacuum boundary can be a quartz plate in front of the lens, or a vacuum window behind the lens. At the other end of the relay lenses or image bundle are a pair of lenses to further de-magnify the image onto a small region of the sensor. Between those lenses, the image is usually collimated for transmission through an optical interference line filter.

GPI optical systems are optimized for maximum light transmission since the higher the transmission, the lower the amount of gas puffing and the lower the potential perturbing effects. Typical optical elements are f/1.4 or lower, and made of quartz for resistance to radiation-induced darkening from fusion plasmas. The coherent fiber bundles are usually made from ordinary glass (e.g., Schott, Inc.), but can be replaced periodically, depending on the neutron or hard x-ray fluence. The in-vessel GPI bundles in Alcator C-Mod were a specially manufactured 5 m long 57 × 57 quartz coherent fiber bundle (Fiberoptic Systems, Inc.), which also have better transmission than glass. The interference filters can have up to 80% transmission at the central wavelength of interest if there are no competing impurity lines within ~10 nm FWHM.

The in-vessel view of the GPI gas puff normally puts the front-end optics close to the plasma edge, so damage to the front-end mirror by the plasma can become a problem. Another practical problem is the slow coating of mirrors and lenses due to plasma-induced deposition. Most GPI front-end optics have a movable shutter to minimize coatings when the GPI is not in use. When this is not possible, the optics can be protected by a front-end tube to reduce coating from angles outside the telescope viewing angle, as in Alcator C-Mod.[14] The balance between optical access and optics damage is normally resolved by trial-and-error on each machine since the in-vessel optics are not movable (at least so far).

C. Detectors

To image edge turbulence in magnetic fusion devices, the light detectors need to have a time resolution of less than ~10 μs and preferably ~1 μs. This can be done with either fast cameras or discrete arrays of photodiodes or photomultiplier tubes. As usual there is a trade-off between the number of channels, the sensitivity of each channel, and the cost, which determines the optimal detector approach for each application.

Commercial fast cameras (e.g., from Vision Research, Inc. or Photron, Inc.) can presently record ~64 × 64 pixel images at framing rates of up to ~400 000 frames/s, which is sufficient to make images such as those in Figs. 3 and 4. However, the pixels in these camera chips are small (~20 μm) and have a relatively low quantum efficiency (~30%), so their optical sensitivity and signal/noise performance are limited. However, these cameras are excellent for detecting the 2-D structure and motion of the turbulence in the brightest region of the GPI gas cloud, which is generally near the magnetic separatrix. Intensified cameras have been tried but do not have significantly better signal/noise than internally cooled un-intensified fast cameras.

An alternative GPI detector is the avalanche photodiode (APD) array, whose detectors can have a larger size and higher quantum efficiency (~80%) than camera pixels. APDs have a variable internal gain. This allows some flexibility in tailoring the gain to the light level incident on a given detector, but requires that the APDs be temperature stabilized, although not to cryogenic temperatures. The internal gain process creates additional noise, lowering the effective quantum efficiency. Nonetheless these detectors have the best signal-to-noise ratio within a certain range of photon flux, ~3 × 10^8-10^{11} photons/s.[75] Thus in those regions of low GPI brightness this detection system has significantly better signal-to-noise ratio than the fast cameras. This is observed in C-Mod where both systems view the same gas puff, and the APD-based array is able to "see" regions of lower emission, in particular into the hotter denser regions inside the LCFS.

The APD arrays used at Alcator C-Mod are operated at a sampling rate of 2 MHz (compared to 0.4 MHz for the camera). Commercial APD arrays (Hamamatsu Photonics) are packaged in arrays of 4 × 8 detectors. One of the C-Mod systems utilizes a close-packed array of 9 × 10 fibers in the focal plane of the optics viewing the outboard midplane region. The fibers are routed to three such APD arrays, with thin interference filters placed between the fibers and the APD arrays. The 9 × 10 fiber array views a ~4 cm × 4 cm area in the plasma in front of the GPI nozzle. Thus the spatial resolution of the APD-based system is considerably less than the camera, but the APDs can measure much lower gas puff signals with good signal-to-noise at higher frequencies than the camera. For example, at 0.9 cm inside the separatrix, the camera and APDs

have a similar frequency spectrum up to ~30 kHz, but noise dominates the camera signal above this frequency (at a framing rate of 400 kHz), whereas the APD can resolve the spectrum up to its noise floor at ~1 MHz. However, at 0.2 cm outside the separatrix in the same shot, where the GPI signal level is larger, the camera can resolve above its noise floor up to ~100 kHz. There is also a very high cross correlation (>0.9) between the camera and APD signals when viewing the same location outside the separatrix.

A third detector is the photomultiplier tube, which has been used in TPE-RX,[76] RFX-Mod,[77] and NSTX.[78] Phototmultipier tubes have lower quantum efficiency (~10% at the wavelengths of interest), but can be operated with higher electron gain than APDs, and can operate at comparable frequencies. For example, the RFX-Mod system uses two 16 channel PM tubes to form three linear fans through the gas cloud covering 7 cm toroidally × 4 cm radially, and digitized at 10 MHz. The resulting 32 channel data have been tomographically inverted to reconstruct localized structures.[79]

Each of these detectors is somewhat sensitive to the neutron and x-ray radiation and electromagnetic fields of magnetic fusion devices. The fast cameras appear to be relatively insensitive to these external noise sources and can operate within a few meters of outer wall of most present day plasma devices, which is required by the limited length of the coherent fiberoptics or relay lenses. The Phantom cameras (Vision Research, Inc.) operate in magnetic fields of ~0.1 T on C-Mod without magnetic shielding. APD arrays are not sensitive to magnetic fields, but will be affected by neutrons if the neutron flux is high enough. Photomultipliers are more sensitive than the cameras or APDs to both radiation and magnetic fields, but, like APD-based systems, can be operated at longer distances from the machines using discrete quartz fibers, with detectors mounted inside magnetic and neutron/gamma shielding.

An ultimate limit to GPI detection is the number of photons in each spectral line emitted prior to the ionization of an incoming neutral atom, commonly called S/XB. For example, if there were (1/15) Balmer-α photons/ionization, as obtained from the "collisional radiative" model for NSTX conditions,[80] as described in Sec. II F, a deuterium gas puff of ~10^{20} D atoms/s would emit ~ 6×10^{18} Balmer-α photons/s, of which ~6×10^{14} s^{-1} would enter the front lens of a typical GPI optical system (f/1.3 lens with a 25 mm focal length at 50 cm from the cloud). If a detector pixel views ~10^{-3} of the area of the emission cloud (to obtain ~1000 active pixels per image), it would then see ~6×10^5 (photons/pixel)/μs. Assuming a photon detection efficiency of ~0.1, this flux would be large enough to obtain ~0.3% photon noise over an integration time of 2 μs, which should be sufficient to resolve plasma light fluctuations as low as ~1%. Additional information about S/XB values for other plasmas can be obtained in Refs. 81 and 82.

D. Calibrations

GPI diagnostics normally do not use the absolute gas puffing rate or absolute brightness of the gas cloud to measure the edge turbulence since the amount of gas or cloud brightness does not (or should not) affect the turbulence properties. However, the GPI gas flow is usually calibrated to compare it with standard gas puff fueling systems, and the brightness is sometimes calibrated to validate the neutral transport codes used to predict the light emission.[80]

The total gas flow from a given puff can be measured without the plasma by the rise in vessel pressure with the pumping temporarily shut off, and checked by the decrease in pressure of the GPI gas reservoir at each puff. The time dependence of the gas puff can be inferred from the time dependence of brightness seen in the GPI, but has not yet been directly measured. The angular distribution of the GPI gas puff was measured in a test chamber for the TEXTOR,[46] but not (to our knowledge) *in situ.* The absolute sensitivity and spatial dependence of the GPI light detectors can be calibrated using a standard light source with the optical filter of interest, located either in a test stand or inside the vessel. The spatial registration and optical resolution of the GPI field of view in the vessel are usually measured using a 2-D (or 3-D) test patterns attached to the gas puff nozzle during a machine opening.

Figure 8 shows a comparison of the observed GPI light emission during a quiescent NSTX H-mode plasma with a simulated GPI camera image produced by the neutral transport code DEGAS 2.[80,83] For this comparison, the gas manifold in the simulation is represented in 3-D as ten squares aligned with the pitch of the actual manifold. Electron temperature and density profiles from Thomson scattering are mapped into the GPI field of view using an EFIT (Equilibrium FITting) magnetic equilibrium. As the D_2 molecules introduced at the simulated manifold penetrate the plasma, they undergo ionization, dissociation, and elastic scattering. The product atoms are then tracked through the plasma and interact with it via ionization and charge exchange, and the resulting 3-D GPI cloud shape is calculated, including recycling from the nearby walls. The Balmer-α photons associated with these processes (Sec. II F) are accumulated into a synthetic camera image constructed from the spatial calibration data. The resulting 2-D spatial distribution of the GPI light agrees quite well with the calculated distribution, and the absolute brightness agrees to within ~50%. This agreement represents a validation of the GPI calibrations and the DEGAS 2 code for the interpretation of GPI Balmer-α light emission, but only with respect to the time-averaged light emission (i.e., not the turbulence). A similarly good level of validation of DEGAS 2 for the 2-D GPI images in helium (587.6 nm) was found for NSTX, but without an absolute calibration.[65]

E. Special features of various GPI systems

This section briefly notes some special features of the GPI diagnostic systems listed in Table I. For further details such as optical system layouts, the reader is referred to the references cited for each device (listed mainly in alphabetical order).

On the Alcator C-Mod tokamak in the US, there were four different GPI sightlines, which had either Phantom cameras or APD detectors.[14–16,45,55,57,62,84,85] The GPI telescopes were mounted onto the interior vessel wall, with a vacuum break
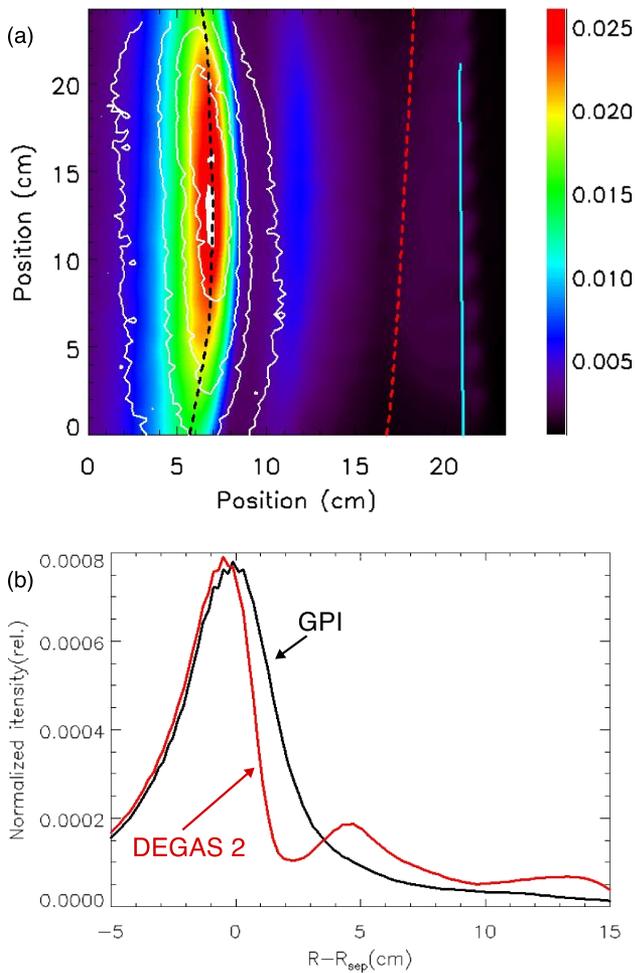
FIG. 8. Comparison between the time-averaged Dα light emission measured in NSTX and the calculated emission in the DEGAS 2 simulation of the NSTX edge plasma and the GPI view. [Reproduced with permission from Fig. 4 of Cao *et al.*, Fusion Sci. Technol. **64**, 29 (2013). Copyright 2013 American Nuclear Society.] The color contours are the DEGAS 2 results and the equally spaced white contours are the GPI results, the leftmost dashed line is the separatrix, the rightmost dashed line is the limiter shadow, and the nearly vertical line is the gas manifold. The 1-D profiles are obtained by normalizing the 2-D data to the sum over all pixels and then averaging over vertical pixels. The horizontal coordinate is mapped to the outer midplane separatrix.

just behind the imaging lenses. The in-vessel quartz fiberoptics were enclosed in flexible stainless steel vacuum bellows, and the light was brought out through windows to the detectors. One camera and one APD array viewed the same outer midplane gas puff. One APD array viewed a puff on the high field side midplane, where fluctuation levels were low compared with the low field midplane, and one camera viewed a gas puff in the region just outboard and above the lower divertor X-point.

The ASDEX tokamak in Germany made the first use of a localized gas puff to make visible emission measurements of edge turbulence.[10,11] Good agreement was found between the turbulence correlation lengths and velocities as measured by the 16 channel photomultiplier detector array and the Langmuir probe fluctuation profiles in the SOL. On the newer ASDEX-Upgrade tokamak in Germany, a Phantom camera was used to measure 2-D images of the turbulence, and a synthetic diagnostic of field-aligned filament geometry used for

interpretation of GPI data.[47] The GPI results were similar to those made with a Li-BES diagnostic.[86]

The Experimental Advanced Superconducting Tokamak (EAST) in China has installed a dual GPI system with two views located ±50° poloidally with respect to the outer midplane, in order to evaluate the up/down symmetry of the turbulence.[51,87–89] The glass fiber bundles are shielded by molybdenum tubes of 10 mm thickness to prevent darkening due to the large hard x-ray flux during lower hybrid current drive (LHCD).

On the Heliotron J stellarator in Japan, the GPI gas puff is located nearby a hybrid Langmuir/magnetic probe for evaluation of cross correlations with light fluctuations.[90,91] On the Gamma 10 mirror machine in Japan, the GPI puff emission was compared with DEGAS neutral simulation code in the mirror machine geometry.[92,93]

On the NSTX spherical tokamak in the US, a single GPI sightline views a gas puff manifold located just above the outer midplane through a re-entrant window port.[12,13,44,52–54,58,78,80,94] This sightline has a wide angle field of view covering ∼30 cm in the poloidal direction and ∼24 cm in the radial direction.

On the RFX-Mod reversed field pinch device in Italy, a single GPI puff at the outer midplane was viewed using photomultiplier arrays from three directions with a two-mirror system, and interpreted using tomographic inversion.[77,79,95–98] The light fluctuations seen with GPI were compared with a thermal helium beam line ratio diagnostic of density and temperature fluctuations made using the same helium gas puff. On the TPE-RX field reversed pinch in Japan, the GPI system was similar to that in RFX-Mod, and there was a retractable Langmuir probe array at the same location as the GPI gas cloud for cross-comparison.[102,103]

On the TEXTOR tokamak in Germany, a 100-hole GPI puff nozzle provided a low divergence gas cloud for improved spatial resolution.[46,99,100] The GPI optics used quartz relay lenses, and the detector was a 300 frame intensified PSI-5 camera. On the TJ-II stellarator in Spain, the neutral gas cloud created by recycling from the limiters was viewed by fast cameras, and double imaging was made with an intensified camera to detect a fine-scale turbulence structure with an exposure time as low as 0.1 μs.[29,30,101] Finally, on the TORPEX toroidal plasma device in Switzerland, an intensified tangential view was interpreted using tomographic image reconstruction, and similar fluctuations were seen in visible light emission and Langmuir probes.[26,27]

IV. CROSS-CHECKS OF GPI DATA

The GPI diagnostic can relatively easily provide highly resolved space vs. time data on plasma edge turbulence in magnetic fusion devices. Before discussing some of the GPI diagnostic issues in Sec. V, this section reviews cross-checks which have been done to compare the GPI data with edge turbulence data from other diagnostics.

Note that GPI data are already being used to test edge turbulence simulation codes using synthetic GPI diagnostics.[3,62,104] However, since these turbulence codes are very complex and not yet "validated," they cannot be used to

check the GPI data itself. There also seems to be no experimental configuration in which the GPI diagnostic can be "benchmarked" against known plasma fluctuations since even the simplest magnetized plasma instabilities are nonlinear and difficult to understand quantitatively. Thus we are left with cross-checking the GPI data with other edge turbulence diagnostics, each of which each has its own limitations and difficulties in interpretation.

A. GPI vs. Langmuir probes

Langmuir probes have been the most common diagnostic for edge plasma turbulence in magnetic fusion devices since they are easy to build and have a high bandwidth (∼1 MHz) and good spatial resolution (∼0.1 cm). Fluctuations in the ion saturation current are usually interpreted as $\delta I_{sat} \sim \delta(n_e T_e^{1/2})$, and the effect of density and electron temperature fluctuations can sometimes be measured separately.[105–107] However, there are usually only a few probes at any given location, and such probes may locally perturb the plasma (usually not well documented).

Many comparisons have been done between light emission fluctuations measured without gas puffing and I_{sat} fluctuations in magnetized plasmas, e.g., at Caltech,[8] TOR-PEX,[27] CSDX,[23] TJ-K,[32] and MAST.[34] These have generally shown a high cross correlation of I_{sat} and visible light fluctuations, even without the explicit line filtering or the localization due to GPI, presumably due to the roughly linear dependence of both diagnostics on the plasma density fluctuations.

The first GPI-type measurements in the SOL of ASDEX showed similar frequency spectra and poloidal correlation lengths between Balmer-α fluctuations and Langmuir probes.[11] Early GPI measurements in the SOL of Alcator C-Mod also showed that the spectra and relative fluctuation levels seen by GPI were similar to those of a Langmuir probe at the same radius.[14,16] Early NSTX results also showed a close similarity between GPI and Langmuir probe spectra and fluctuation levels,[94] and later results showed a close similarity between GPI and probe turbulence correlation lengths and velocities.[108] Since these probe and GPI measurements were not made at the same locations in these plasmas (and sometimes not in the same shots), more precise cross-checks were not possible.

Somewhat more quantitative are cross correlations measured between fluctuations in GPI and probes on the same magnetic field line, which are made using field line mapping codes along with a search for the best correlation within the 2-D GPI field of view. As illustrated in Fig. 9, on Alcator C-Mod there was a ∼76% cross correlation between GPI emission from an outer midplane view and I_{sat} fluctuations from a reciprocating probe ∼3 m away along the same B field line (with >90% cross correlation for shorter time series), and ∼81% cross correlation between midplane GPI emission and I_{sat} at a divertor-target probe.[84] In NSTX, cross correlation of GPI images with I_{sat} fluctuations was ≥0.8 for five fixed Langmuir probes in the SOL located ∼1 m along B,[109] similar to the Alcator C-Mod results. These cross-checks show that the GPI and probes are basically measuring similar plasma pressure fluctuations, although the mixture of density and temperature fluctuations measured by the each of these two diagnostics is somewhat different.

Local cross-checks between GPI and probes within a turbulence correlation length are desirable but difficult due to limited diagnostic access. However, this was tried on the TPE-RX reversed field pinch where Langmuir probes could be moved near to the GPI gas nozzle.[102,103] The cross correlation between GPI and I_{sat} fluctuations at about the same radius was ∼55%, with a near-zero time delay between them, roughly as expected if both were measuring density fluctuations. A combined GPI and Langmuir probe was also used on the Heliotron J stellarator, where turbulent bursts of I_{sat} fluctuations were accompanied by filamentary structures seen along the B field in GPI.[90,91] To our knowledge no local comparisons of GPI and probes have been made in a tokamak although a high correlation was found between passive imaging of edge filaments and nearby probe signals in the Caltech[8] tokamak and in MAST.[34]

B. GPI vs. beam emission diagnostics

Another type of turbulence diagnostic is based on the light emission from injected high energy neutral particle beams, instead of the injected cold gas used in GPI. The principle is similar: the line emission from the neutral beam species depends on the local plasma parameters, especially the electron density, and can be used to measure the local electron density fluctuations. There are two main variants of this
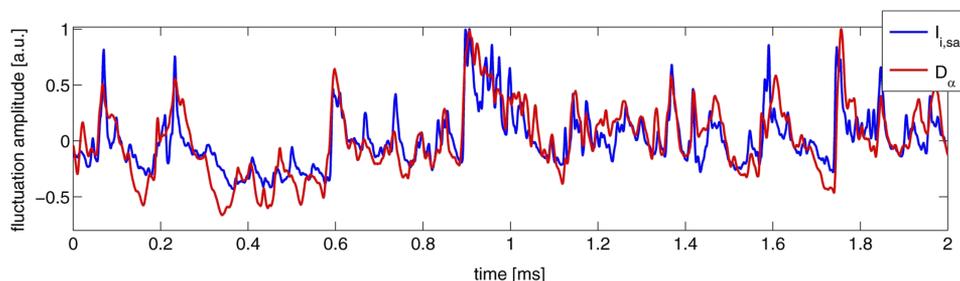

FIG. 9. A ∼2 ms long time series of ion saturation current fluctuations measured with a reciprocating probe in Alcator C-Mod (blue), overlaid with a GPI signal from a single view within the 2-D array of APD views at outer midplane. [Reproduced with permission from Fig. 5 of Grulke *et al.*, Nucl. Fusion **54**, 043012 (2014). Copyright 2014 IOP Publishing.] These two diagnostics sample the same flux-tube, but displaced by ∼2.8 m along B. It is clearly seen that fluctuation events are observed by both diagnostics, and large-amplitude events especially can be directly identified in both traces. The cross-correlation amplitudes between the GPI emission and $I_{i,sat}$ of over 75% are found in some cases. A small −1.5 ± 0.5 μs time delay maximizes the cross-correlation between the two time-series.

diagnostic, one using a low power (~200 W) lithium beam spectroscopy (Li-BES), such as in ASDEX-Upgrade[110] and the other using a high power (~1 MW) deuterium heating beam (BES), such as used in TFTR,[111] D-IIID,[112] NSTX,[113] and MAST.[114]

Lithium BES was used to measure density fluctuations in the SOL of the W7-AS stellarator, and it was found that "all parameters of the SOL turbulence seen by the Li-beam diagnostic agree with the Langmuir probe and H_α measurements."[115] Both GPI and Li-BES were used to evaluate the properties of discrete blobs in the SOL of ASDEX-Upgrade in separate papers.[47,86] The results of the two diagnostics appear to be very similar, e.g., with radial blob widths of ~1 cm and radial blob speeds of ~0.3 km/s; however, it is difficult to make a direct comparison since these measurements were made at different locations and on different discharges.

Edge turbulence measurements using BES and GPI were directly cross-checked in NSTX.[116] This comparison was made using the same discharges and poloidally (but not toroidally) overlapping edge and SOL regions near the outer midplane. Strong cross correlations were observed (~70%), and high cross-coherence was seen for frequencies between 5 and 15 kHz. Good agreement was also found between correlation length estimates, de-correlation times, and structure velocities in the two diagnostics. However, the relative fluctuation levels seen in GPI exceeded BES fluctuations by a factor of ~9, which was well outside the range of expected uncertainties. In addition, the BES mean intensity was found to be sensitive to the GPI neutral gas puff, and BES normalized fluctuation levels for frequencies between 1 and 10 kHz were sometimes observed to increase during the GPI puff. These discrepancies have not yet been understood or resolved.

C. Other diagnostic cross-checks

Edge turbulence is also measured in magnetic fusion plasmas by electromagnetic scattering, reflectometry, or phase contrast imaging (PCI). These methods are entirely non-perturbing since negligible EM wave power is absorbed by the plasma, but the interpretation of these diagnostics is difficult and these measurements are usually not well localized spatially. For example, the frequency spectra of an edge reflectometer at the outer midplane of NSTX were found to be very similar to a GPI channel at the same radius.[94]

As noted in Sec. II C, GPI can measure properties of edge quasi-coherent modes, in particular poloidal wavenumbers, radial localization, and (lab) frequency spectra. On C-Mod, the Quasi-coherent Mode (QCM) present in the edge of Enhanced-D_α H-mode plasmas is observed with diagnostics sensitive to edge density fluctuations, i.e., GPI, a reciprocating Langmuir probe, PCI, and reflectometry.[50] All observe the same peak frequency for the mode. The GPI, probe, and PCI diagnostics observe a poloidal wavenumber, k_{pol}, that is consistent with a field-aligned mode whose k_{pol}, at the midplane of ~1.5 cm^{-1}. The reciprocating probe and GPI measure the radial location and width of the mode. The measured widths are the same (within radial resolution),[107] but the absolute radial location of the mode differs by ~5 mm.[107,117] The absolute location

determination depends on the EFIT equilibrium reconstruction to map the measurements to a common radial grid, but the difference is somewhat outside of the estimated EFIT and registration uncertainties. The reasons for the differences are thus still under investigation.[118]

Edge electron density and temperature fluctuations can also be measured using a thermal helium beam (THB) diagnostic, which is similar to GPI but measures the intensity ratios of three neutral helium lines. The THB in RFX-Mod is located near to the GPI diagnostic.[59,98] A conditional sampling study of positive density events δn_e (i.e., blobs) within a slowly rotating helical mode in this RFP showed the local δT_e perturbation to be *inversely* correlated with δn_e, such that $\delta T_e/T_e \propto (-0.3 \, \delta n_e/n_e)$ for radii r/a ~0.95-0.99. This is apparently different than the relationship between δT_e and δn_e in tokamak SOL, where δT_e and δn_e are positively correlated.[106–108] This relationship is important for the interpretation of GPI, as discussed further in Sec. V B.

A cross correlation coefficient up to ~80% was found between GPI fluctuations at the outer midplane and LiI 670.8 nm line emission fluctuations measured at the surface of the divertor target plate in NSTX.[39] This high cross correlation was explained by magnetic field line mapping, in which a blob at the outer midplane SOL was mapped along B to a helical spiral which covers a large toroidal angle at the divertor plate. The result again suggests that GPI is responding to local density fluctuations, which cause similar line emission fluctuations in all species.

V. GPI INTERPRETATION ISSUES

This section discusses some issues which can affect the interpretation of GPI measurements in magnetic fusion devices. These are to some extent open questions and will not be completely resolved here, but additional calculations and/or experiments are suggested.

A. Uniformity of the gas cloud

The GPI gas puff flows typically from a gas reservoir at ~1 bar through a nozzle of ~1 mm diameter into a vacuum chamber at <10^{-6} bar. Is the resulting neutral gas density highly uniform at the GPI measurement location or does some gas flow instability cause local fluctuations in the neutral cloud density which could be misinterpreted as plasma fluctuations? Note that only the time-dependent non-uniformities will affect the GPI analysis, since the GPI data are usually normalized by the time-averaged cloud emission to remove the expected systematic spatial cloud non-uniformities.

The most detailed experimental study of the neutral gas cloud in GPI was done for the TEXTOR system, in which angular distribution of deuterium gas was found to be smoothly varying at a distance of 20 cm from the nozzle exit using a quadrupole mass analyzer.[46] The gas flow regime had an estimated Knudsen number Kn ~ 0.6, i.e., nearly collisionless flow, but possible time-dependent non-uniformity was not discussed. More extensive gas cloud measurements have been made for high-Z noble gas targets which are used for high intensity laser-plasma interaction experiments.[119–121]

Although these gas targets were spatially uniform far from the nozzle tips (as desired for those experiments), some evidence for small-scale vortex motion very near the nozzle tips was observed although the time dependence was not measured.[119] In rare instances, some vortex or arc-like structure was seen in the GPI light emission very near a single gas nozzle tip in the early Alcator C-Mod data.

In GPI systems, the neutral gas cloud (without any plasma present) will most likely be spatially uniform in regions where the neutral-neutral mean collisional free path L_o of the gas atoms or molecules is larger than the size of the structures to be measured, independent of the gas source. Assuming $L_o \sim 1/(\sigma n_o)$, where $\sigma \sim 7 \times 10^{-16}$ cm^2 is the hard-sphere collisional cross for helium or deuterium molecules and n_o is the local gas density, the GPI cloud should therefore be uniform on the scale of $L_o > 100$ cm at $n_o \sim 10^{13}$ cm^{-3}, which is the maximum estimated gas density in a typical GPI cloud (Sec. V D). Thus cloud non-uniformities are unlikely to affect the interpretation of cm-scale structures in GPI, at least far from the nozzle tips.

Substantial indirect evidence also suggests the absence of GPI cloud non-uniformity effects on the measured turbulence, for example, sudden quiescence in the images at H-mode transitions (e.g., Fig. 2), the high cross correlation between GPI and remote probe measurements (Sec. IV A), the *outward* movement of blobs in the SOL,[48] and the absence of a dependence of GPI results on the gas puffing rate.[58] Nevertheless, it would be interesting to measure directly the gas cloud uniformity on the space and time scales of edge turbulence without plasma, as done for gas puff laser targets,[119] and also to calculate the expected gas cloud uniformity using a realistic fluid/molecular dynamics simulation code.

B. Relationship to density and temperature fluctuations

As discussed in Sec. II F, the visible line emission fluctuations δI measured by GPI depend on both the electron density and temperature fluctuations, so that without an independent knowledge of the relationship of δn_e to δT_e, it would not be possible to infer either of them directly from δI. However, if there is a high cross correlation between δn_e and δT_e, then the *cross correlation properties* of δI should be nearly the same as those of δn_e. This was shown by numerical examples in which the autocorrelation time of δI was nearly the same as that of $(\delta I)^\gamma$ for $-2 < \gamma < 4$.[94] In a more general imaging context, the independence of cross correlations on γ is why the apparent size and the motion of objects are not greatly affected by nonlinear distortions in the contrast setting of video displays or by the nonlinear response of the eye.

However, the *relative fluctuation levels* $\delta I/I$ seen in GPI will depend on the both $\delta n_e/n_e$ and $\delta T_e/T_e$ (as it does also with Langmuir probes), so $\delta n_e/n_e$ cannot be inferred from $\delta I/I$ without knowledge of the emission "exponents" (see Sec. II F), even if δn_e and δT_e are well correlated. For example, the increased sensitivity of HeI emission to δT_e at very low T_e (see Fig. 6) implies that δI fluctuations can be significantly affected by relatively small δT_e.[122] There may also be regimes where correlated fluctuations of density and temperature may

be "invisible" due to their canceling sensitivities.[123] If δn_e and δT_e are uncorrelated, the correlation properties of δI will be a weighted mixture of both, and may be a representative of neither.

Despite these limitations, the GPI results have been directly compared with the turbulence theory and simulation using a synthetic diagnostic code which calculates the expected GPI light emission from the n_e and T_e dependences shown in Fig. 6. In the turbulence simulations done so far, it has generally been found that δT_e and δn_e are well correlated since both are dominated by local ExB drifts, so that the turbulence properties calculated using the synthetic diagnostic for δI are similar to those of δn_e.[3,62,104,124] In these papers there has been a fairly good agreement (~factor-of-two) between the synthetic GPI diagnostic results based on the turbulence simulations and the actual GPI measurements. However, it is always desirable to cross-check GPI measurements with diagnostics which measure the density or temperature fluctuations, e.g., probes in the SOL.

C. GPI line emission processes

As described in Sec. II F, the usual interpretation of the GPI diagnostic assumes that the measured line emission from the gas cloud does not contain significant contributions from molecular processes or impurities, instantaneously responds to changes in the plasma density and/or temperature, and is optically thin, i.e., that one can neglect absorption of light by the cloud itself or by intervening neutral atoms.

Dissociation of deuterium molecules and their ions does result in excited products, some in the n = 3 state, which can then radiatively decay to produce Balmer-α photons. The simplest means of accounting for them is as additional, independent contributions to the total light emission that scale linearly with the D_2 and D_2^+ density.[17,80] By assuming that the molecular ions dissociate instantly upon D_2 ionization, the D_2^+ density can be expressed as the ratio of its formation to destruction rates times the D_2 density. The total photon emission rate per molecule, the "Molecular Contributions" curve in Fig. 6(a), can then be obtained from the rates in the literature.[125] The molecular density in the vicinity of the emission cloud can be independently determined through the Fulcher band spectroscopy.[126–128]

Consistent molecular and atom density profiles can be obtained via neutral transport simulations of GPI experiments, such as those described of Alcator C-Mod[17] and NSTX.[80] These works determined the fraction of Balmer-α light coming from molecular processes using the rates underlying the "Molecular Contributions" curve in Fig. 6(a) and found it increasing from >10% at the small R edge of the emission cloud, to ~30% at the emission peak, and to >50% at the large R edge of the cloud. Although not large enough to invalidate the use of Eq. (3) for the qualitative interpretation of Balmer-α GPI data, these contributions must be accounted for in quantitative applications and in model validation tests. However, the rates for the relevant processes are not well established, e.g., different sets of data are used in Refs. 129 and 130. Moreover, Fantz *et al.*[127] and Heger[131] concluded that D_2 and D_2^+, along with their vibrationally excited states, should be

incorporated into a comprehensive collisional radiative model together with D and D$^+$, and such models and the issues associated with their construction have been described.[132,133] Janev *et al.* have reviewed the current state of the required data and concluded that although much of these data are available, more is needed.[134]

The time response of the GPI emission can be broken down into three components: (1) transport time scales for the emitting atoms, (2) radiative decay time of the excited state, and (3) time scale for the atomic system to reach equilibrium. The distance traveled by the emitting species in, say, 1 μs ranges from 0.1 cm for a thermal helium atom or deuterium molecule to 5 cm for a 30 eV deuterium atom. However, the more relevant time scale is that for radiative decay. For both the deuterium Balmer-α and He 587.6 nm lines, the radiative decay times are ~0.01 μs, effectively instantaneous. Over that interval, even the 30 eV atom moves only 0.1 cm. At electron densities sufficiently low for the coronal equilibrium approximation to be valid ($n_e < 10^{11}$ cm^{-3} so that f $\propto$ n_e), the time scale for the excited states to reach equilibrium is set by that of radiative decay.[135]

The situation is more complex at the higher densities more typically encountered in GPI applications. A direct investigation of this question was undertaken in Ref. 65 where the accuracy of the time response of Eq. (3) for helium was assessed. More specifically, the presence of the 2^1S and 2^3S metastable states points to a possible need for a more complex collisional radiative model in which these states are treated explicitly.[72] Application of the eigenvalue analysis developed in Ref. 132 to helium suggests that the simpler model (Eq. (3)) is capable of reproducing sub-microsecond time scales for plasma conditions typical of the center of the emission cloud. In a more specific numerical test with plasma parameters evolving on a 10 μs time scale, typical of turbulence auto-correlation times, the light emission from the two collisional radiative models could not be distinguished from that obtained by integrating the full set of atomic state equations. Ma *et al.* looked at the response of the helium system over a wide range of frequencies and found that the simple CR model is adequate at MHz and slower frequencies.[136] More complex behavior was found at higher frequencies.

The temporal characteristics of the hydrogen system were analyzed in Ref. 132. In the absence of molecules, the response time scale for hydrogen is again expected to be ~0.01 μs, much shorter than turbulence time scales. The addition of molecules undoubtedly introduces longer time scales although we are not aware of a quantitative characterization beyond that described in Ref. 132. In that work, he showed the atom density was evolving on a 10 μs time scale following the introduction of ground state molecules into a 10^{13} cm^{-3}, 7 eV plasma, implying that the emitted light may be varying on turbulence time scales.

During normal operation of magnetic fusion devices, there are no significant contaminating lines from other species within the spectral line width of the GPI neutral Balmer-α or helium 587 nm lines. There is a CII line (657.8 nm) within 2 nm of Balmer-α. However, the emission from the GPI puff should overwhelm the intrinsic line emission from the edge plasma.

D. GPI optical thickness

This section describes in some detail the issues concerning optical self-absorption of the spectral lines of deuterium and helium in plasmas. The conclusion is that the visible lines used for GPI are normally optically thin in magnetic fusion edge plasmas, so self-absorption is not a problem for the interpretation of GPI in present experiments.

The rate at which photons are resonantly absorbed is proportional to the density of atoms in the lower level of that atomic transition. Consequently, lines starting from the ground state are the first to become opaque as the gas density is increased. The effects of the trapping of hydrogen Lyman series lines in recombining divertor and MARFE (Multifaced Asymmetric Radiation From the Edge) plasmas have been investigated by several groups, e.g., Refs. 137–142. For helium, similar work has been done on linear devices[143–148] and tokamaks.[66,149]

To obtain a rough estimate of the importance of radiation trapping for GPI, one can evaluate the line center absorption coefficient for the Doppler broadened j $\rightarrow$ k transition [e.g., from Ref. 140] χ_0,

$$\chi_0(\text{cm}^{-1}) = 1.08 \times 10^{-2} f_{jk} \lambda_{jk}(\text{nm}) N_j(10^{13}\text{cm}^{-3}) \left[\frac{\mu}{T_j(\text{eV})}\right]^{1/2},$$

(7)

where f_{jk} is its absorption oscillator strength, λ_{jk} is its wavelength, N_j is the density of state j, T_j is its temperature, and μ is the mass of the emitting atom relative to that of a proton. We note first that the lines used (Balmer-α and 587 nm) are optically thin because the density appearing in Eq. (7) is that of an excited state, much smaller than the ground state density. However, it is still important to check the opacity of the primary transition to the ground state (Lyman-α and the 1^1S-2^1P line (58.4 nm) in He). For DEGAS 2 simulations of NSTX deuterium GPI, the peak atom density in the vicinity of the emission cloud at the relatively high peak puff rate of ~6.6×10^{21} D/s is estimated to be 5×10^{12} cm^{-3} and the atom temperature ~5 eV.[58,80] For the Lyman-α line, $f_{12} = 0.4162$, $\lambda_{12} = 121.6$ nm, giving $\chi_0 = 0.17$ cm^{-1}. The thickness of the gas cloud in the direction of the detector is L ~ 15 cm, giving an optical depth of χ_0 L = 2.6. While this is >1, our evaluation uses the peak density, both in time and space. Moreover, the much smaller radial thickness of the cloud, ~3 cm, is a relevant consideration. Consequently, radiation trapping is likely inconsequential in this application.

For the same gas puff rate, the effects for helium can be much greater for two reasons. First, the helium densities are typically about an order of magnitude larger than those of deuterium because the latter atoms are products of dissociation and so have higher energy and longer mean free paths in the scrape-off layer. Second, the helium temperatures are much lower due to the lower source energy (~0.03 eV for He vs. ~3 eV for D) and the relative inefficiency of He-D$^+$ elastic scattering compared with resonant charge exchange. To make a quantitative comparison with deuterium, we again examine DEGAS 2 simulations of NSTX GPI and find a helium density of 6×10^{13} cm^{-3} at the emission cloud assuming a peak puff rate equal to that of D$_2$ and a temperature of 0.1 eV. For the

1^1S-2^1P He transition (not normally used in GPI), $f_{12} = 0.276$, $\lambda_{12} = 58.4$ nm, yielding $\chi_0 = 6.61$ cm^{-1}. Even with the radial width of 3 cm, one gets an optical depth $\chi_0 L = 19.8 >> 1$, implying that absorption of this XUV line in this cloud is significant.

The actual helium puff rate used in GPI experiments such as Alcator C-Mod,[85] NSTX,[13] and EAST[87] has typically been ~ 0.8-6×10^{20} atoms/s, i.e., at least an order of magnitude lower than the NSTX D$_2$ puff rate assumed above, which would seem to imply a helium XUV line opacity closer to unity. However, making a conclusive determination requires accounting for the details of the GPI system as well as the plasma parameters. DEGAS 2 simulations of calibrated He puffs of $\sim 1 \times 10^{20}$ atoms/s into C-Mod plasmas yield peak atom densities of $\sim 6 \times 10^{13}$ cm^{-3} at the nozzle side of the GPI field of view; the He density at the LCFS is smaller by an order of magnitude. Thus, even with the lower puff rate, there may be trapping of the 58.4 nm resonance line close to the nozzle in the C-Mod case. To understand the apparent discrepancy, one needs to note first that the gas source in C-Mod is more compact than in NSTX (3 cm vs. 30 cm) and second that the emission volume is much closer to the source (2–3 cm vs. 10–15 cm). In contrast, the helium atom density in the EAST GPI has been estimated to be $n_o \sim 10^{12}$ cm^{-3}, too small for trapping of the 58.4 nm resonance line to be significant.

Modeling an optically thick system requires incorporating absorption into the collisional radiative model. The simplest approach is via escape factors [e.g., Refs. 130 and 145] although potentially critical geometry and line shape details may be missed. More sophisticated approaches employ direct Monte Carlo photon transport[142] or a nonlocal thermodynamic equilibrium model with line radiation interactions.[150,151] The net effect of the trapping of ground state transition lines is an increase in the population fractions for all of the excited states [$f(n_e, T_e)$ in Eq. (3)] and of the effective ionization rate of the system. More importantly, photon absorption renders the collisional radiative calculation (which was used to evaluate the emission "exponents" in Sec. II C) non-local, vastly complicating the quantitative interpretation of the light emission. The estimation of photon absorption rates for He puffing can also be obtained combining the measurements of 4-5 emission lines and collisional radiative model;[152] this method does not require trapping radius and neutral temperature.

In summary, these estimates show that the GPI gas cloud is optically thin for the visible deuterium and helium lines used in the present experiments (with the possible exception being the region just in front of the nozzle). In more general situations, e.g., for XUV line emission, the simplest means of ensuring that a GPI system is optically thin is to use a sufficiently small gas puff rate and to favor deuterium over helium.

E. Shadowing of neutral density by turbulence

The usual interpretation of GPI is that the local neutral density of the GPI species is only slowly varying in space and time, and its density is determined only by the gas puff input and by ionization and charge exchange in the plasma. This is the model that produced good agreement with the time-averaged 2-D profile of GPI light emission in Fig. 8. However,

localized n_e or T_e fluctuations within the gas cloud might also modify the instantaneous local density of GPI neutrals via ionization and the other neutral-plasma interaction channels. This effect was previously discussed and simulated as "shadowing" in the context of deuterium GPI in Alcator C-Mod, using the DEGAS 2 Monte Carlo neutral code and *ad hoc* time-independent electron density and temperature perturbations.[17] This shadowing effect in GPI is similar to the edge induced beam noise evaluated for the BES diagnostic.[153]

Alternatively, we can imagine these atomic physics processes as transferring some of the structure of the plasma turbulence to the neutral density. The neutral density and thus the light intensity at those radii will depend on the plasma parameters that have been "seen" by those molecules and atoms en route from the gas nozzle. In GPI, this effect is most likely reduced with respect to the BES diagnostic by those factors which tend to isotropize the effects of turbulence on the GPI neutrals, namely, the random initial gas motion, charge exchange and molecular dissociation (in deuterium), and neutral atom heating (in helium).

A result from the DEGAS 2 simulation of NSTX GPI is shown in Fig. 10, taken from Ref. 17, where in (a) the model includes the shadowing effect, and in (b) does not; the result is that the spatial structure of the emission profile in (a) is smeared out relative to the idealized result shown in (b) and relative to that of the perturbed density. This was also recently revisited using a SOL turbulence simulation code with a mono-energetic, one-directional neutral source model in which the GPI simulation of radial "fingers" in the turbulence model was significantly affected by the shadowing effect in the strong interaction regime, in which the neutral mean free path was smaller than the radial size of the turbulence.[154] The influence of turbulence and blobs on the neutral particle profile has also recently been analyzed in Refs. 155–157.

It is difficult to assess the GPI shadowing effect for specific experimental cases without a realistic edge turbulence model coupled to a 3-D Monte Carlo neutral model such as DEGAS 2 or EIRENE. It may also be necessary to include time-dependent effects since the neutral speed can be near the turbulence propagation speed. Until these simulations are done, the quantitative effects of shadowing on specific GPI diagnostic results are not clear. As far as we know, shadowing effects in GPI have not been identified experimentally. However, they might be found as radial anti-correlations in turbulence cross correlation functions although this could also be caused by correlation properties of the edge turbulence itself.

F. Gas puff perturbation effects

At very high levels of gas puffing, there will at some point be a significant perturbation of the edge plasma, either in electron density or temperature. Therefore the GPI gas puff level is normally chosen to be as small as possible consistent with good GPI signal levels. This GPI puff level is normally much lower than the puff level used for pulsed gas fueling of these devices. The gas puff of GPI can also cause perturbations which may be visible in other diagnostics, for example, in BES (see Sec. IV B) and CHERS in NSTX, if these sightlines are coincidentally near to the GPI neutral cloud.
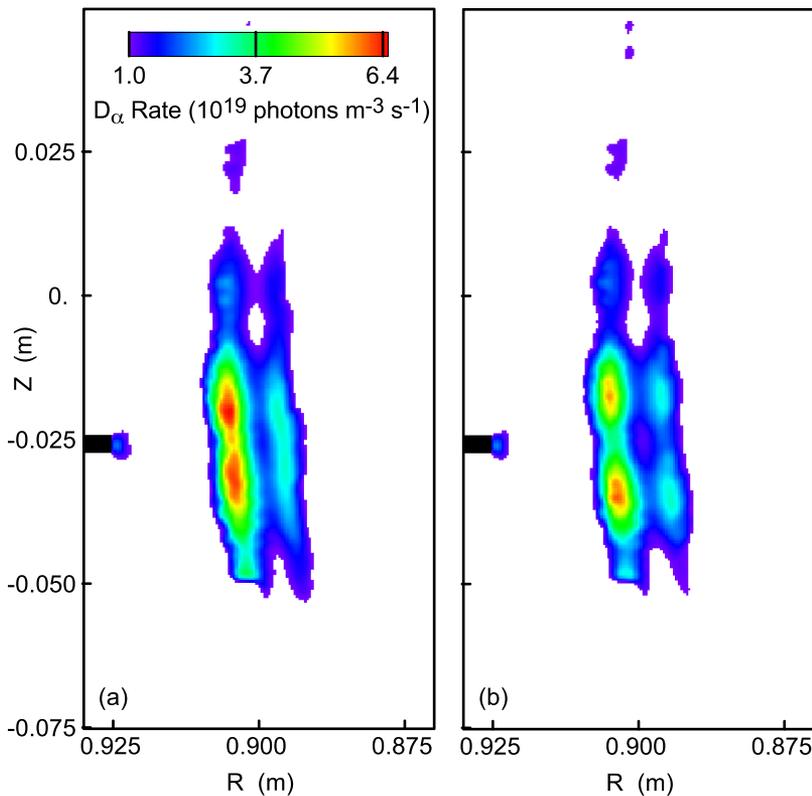
FIG. 10. DEGAS 2 simulations of the Dα light emission patterns in GPI in Alcator C-Mod assuming a strong poloidal and radial modulation of the electron density. [Reproduced with permission from J. Nucl. Mater. **313-316**, 1066 (2003). Copyright 2003 AIP Publishing LLC.] The gas nozzle is shown as a black rectangle in the left. In (a) the shadowing effect of the fluctuations on the neutral density is incorporated, and in (b) the shadowing effect has been eliminated using post-processing. The result is that the spatial structure of the emission profile in (a) is smeared out relative to the idealized result shown in (b) and relative to that of the perturbed density.

A recent study of the effect of a deuterium GPI puff on the NSTX plasma found no significant perturbation of the measurable plasma edge parameters or edge turbulence (as measured by GPI itself) up to the time of the peak GPI deuterium influx rate of ~6.6×10^{21} atoms/s at ~20 ms after the start of the puff.[58] After this time, the GPI gas continued to enter the plasma over ~60 ms, and eventually the edge density and temperature (measured by Thomson scattering) were sometimes perturbed by the GPI puff, depending on the type of plasma. However, no systematic changes in the edge turbulence correlation lengths, correlation times, relative fluctuation levels, or turbulence poloidal velocities as measured by GPI occurred between the very start of the puff at 20 ms before its peak to ~60 ms after the peak. This suggests that the GPI neutrals do not significantly change the flow damping, at least in NSTX. On the TEXTOR tokamak, there was no significant perturbation in the plasma or edge turbulence at their deuterium GPI puff rate of up to ~4.6×10^{20} atoms/s for ~0.5 s.[46]

On the other hand, some small tokamaks such as ADITYA have reported changes in the edge turbulence with gas puffs of ~2×10^{21} atoms/s correlated with a decreases in the edge electron temperature due to radiative cooling.[158,159] On other devices such as Alcator C-Mod when operating at low densities $\overline{n_e} \lesssim 0.8 \times 10^{20}$ m^{-3} or EAST,[87] the normal helium GPI puff of ~10^{20} atoms/s for ~0.2 s caused a significant (≥20%) rise in plasma electron density, probably due to the recycling of helium. A similar or larger rise in density is caused when a deuterium puff is used for GPI in C-Mod.[62] However, as with NSTX, these density rises did not appear to perturb the edge turbulence significantly.

The perturbing effects of the GPI gas puff will depend on the size and density of the device, on the edge plasma transport (which determines the response of the edge to a given particle source), and on the sensitivity of the edge turbulence to the local edge parameters, which tends to be weak [e.g., Refs. 47, 160, and 161]. Thus it is difficult to characterize the perturbing effects of the GPI puff in general terms. There may also be different perturbing effects within the puff cloud itself and remotely on the same field line although fast parallel electron motion tends to strongly correlate the turbulence along B. Specific cross-checks of GPI results with other diagnostics should be made for each device, as described in Sec. IV, and the puff strength should be varied to look for systematic changes in the turbulence vs. puffing rate.

The perturbing effects of the gas puff are also difficult to predict theoretically since they depend of the physics of the edge turbulence, which is not well understood. For example, the effects of neutral atoms on the edge stability and rotation has been discussed for many years [e.g., Refs. 162 and 163], but clear experimental confirmation of these theories has not yet been obtained. The effects of gas puffing on other tokamak edge physics such as ELMs, RF wave heating, and divertor operation can also be interesting and important. Therefore further theoretical modeling and experimental validation on the effect of a gas puff on the edge turbulence and transport is certainly appropriate and is ongoing [e.g., Refs. 163 and 164].

G. Plasma rotation and radial transport from GPI

GPI measures the excitation of neutrals by electrons, so cannot directly measure the velocity of plasma ions. However, if the fluctuations in electron density and/or temperature rotate along with the ion fluid motion (e.g., due to ExB drifts),

then these fluctuations will appear to move in this direction in GPI. To the extent that fluid rotation dominates this apparent turbulence motion, the GPI can measure this rotation velocity, similarly to BES and Doppler reflectometry diagnostics (which also measure the motion of electron fluctuations). This rotation velocity is superimposed on whatever velocity the turbulent fluctuations have in the fluid rest frame, e.g., due to diamagnetic drift motion.

The turbulence poloidal velocity in GPI has been inferred from time-dependent cross correlations, pattern matching, optical flow, and Fourier methods.[165–167] Poloidal rotation is observed in GPI in either in the electron or ion diamagnetic direction, as discussed in Sec. II C. Although there are several difficulties and subtleties in this velocimetry analysis, the observed velocities are near the expected poloidal $E_{rad} \times B$ and/or diamagnetic drift speeds of $V_{pol} \leq 10$ km/s, i.e., far below the ion sound speed. The fine structure in the GPI poloidal rotation in the SOL of Alcator C-Mod has also been associated with radial electric fields driven by ion cyclotron range of frequencies (ICRF) antennas.[168]

Toroidal rotation of plasma ions is also common in tokamaks and stellarators due to toroidally asymmetric neutral beam injection or intrinsic rotation (without any external momentum source). However, in most GPI systems it is not possible to distinguish between the effects of toroidal and poloidal fluid rotation since the toroidal rotation of a helical structure will appear as a poloidal rotation when viewed parallel to the local B. Apparent toroidal rotation of edge turbulence has been observed in the MAST using a passive filament imaging in the toroidal vs. poloidal plane, but it was not possible to distinguish between toroidal and poloidal motion.[34] In NSTX there was a surprising invariance to NBI power of the poloidal rotation in GPI, suggesting that toroidal rotation at the plasma edge was not dominating the turbulence motion seen in GPI.[161]

Parallel rotation (along the magnetic field direction) should not be visible at all in GPI if the turbulence is constant along a field line (i.e., $k_{\parallel} \sim 0$), and if the GPI view is aligned along B. For example, if $k_{\parallel} \sim 1/qR \sim 10^{-2}$ cm^{-1} for drift-type waves inside the separatrix, at parallel rotation speeds of $V_{\parallel} \leq 10$ km/s the GPI would see the parallel structure at $f = k_{\parallel}V_{\parallel}/2\pi \leq 1.5$ kHz, which is at the low end of the normal turbulent frequency spectrum. No clear indication of parallel rotation in GPI data has yet been observed.

Many GPI results have shown radially outward turbulence or blob motion, which is tempting to interpret as radial transport. However, the radial transport due to turbulence actually depends on the local cross correlations of the density, temperature, and radial fluid velocity fluctuations, none of which can be directly measured by GPI. Therefore it is difficult to make direct inferences about turbulent transport using GPI results. However, progress in understanding edge transport can be made by comparing GPI results with synthetic diagnostics from theoretical turbulence simulations, which can then be validated to help understand radial transport.

VI. DISCUSSION

This paper reviewed gas puff imaging (GPI) diagnostics of edge plasma turbulence in magnetic fusion research,

with a focus on the instrumentation, diagnostic cross-checks, and interpretation issues. This section contains a brief summary of this review, along with potential improvements to this diagnostic and suggested directions for further research.

A. Summary

As discussed in Sec. I, the main motivation for GPI is to obtain high space vs. time resolution of the turbulence in the edge of magnetic fusion devices, where the temperature is T_e ~10-100 eV. Passive optical imaging of visible light fluctuations can provide some information on edge fluctuations, but is limited in toroidal devices by the line-of-sight integration over natural emission sources. Thus 2-D imaging of turbulence is more easily done using a controlled neutral gas puff in the GPI configuration.

Sec. II gave an overview of GPI, including the basic geometry and several examples of GPI images. A list of edge plasma measurements which have been made using GPI was presented in Table I. The choices for GPI gas species and spectral line were described, along with limits of GPI spatial resolution. The theoretical dependence of the GPI light emission on the electron density and temperature and its sensitivity to fluctuations was discussed and shown in Figs. 6 and 7.

The GPI gas puff hardware, optics, and detectors were described in Sec. III. The GPI diagnostic is relatively simple and flexible, and has been used in several types of magnetic fusion devices, as listed in Table II. The imaging can be done with commercial high speed cameras, or with arrays of avalanche photodiodes or photomultiplier tubes. The spatial and optical calibration of GPI systems is straightforward.

Section IV described various cross-checks of GPI results with other edge turbulence diagnostics. Similar turbulence properties were found with GPI and Langmuir probes on many devices, and high cross correlation coefficients of ~0.8 were found between GPI and Langmuir probes located on the same B field line. There was also a close similarity between GPI results and other optical diagnostics of edge turbulence.

The main difficulties in GPI concern the interpretation of the results in terms of the local plasma density and/or electron temperature fluctuations. All known issues concerning the interpretation of GPI measurements were discussed in Sec. V, including the uniformity of the gas cloud, the response to electron temperature and density fluctuations, optical line emission and absorption, shadowing of the neutral density by turbulence, gas puff perturbation effects, and rotation and transport effects in GPI. The most subtle issues in GPI interpretation concern the possible effects of the gas cloud on the edge turbulence, and of the edge turbulence on the GPI gas cloud. These effects have not yet been identified in existing GPI measurements, and cannot yet be realistically modeled or predicted theoretically.

In general, the GPI diagnostic can provide excellent space and time resolution of edge turbulence in magnetic fusion plasmas, but only within limitations set by the hardware and uncertainties in the interpretation of the data. Therefore the results should be cross-checked where possible with other edge

turbulence diagnostics as discussed in Sec. IV and should be evaluated for each device with respect to the issues discussed in Sec. V.

B. Potential improvements

Some potential improvements to resolve specific diagnostic and interpretation issues were already mentioned in Sec. V. In this section we summarize and extend this list of potential improvements to GPI hardware and data analysis.

The spatial resolution of most GPI systems could be improved by using a collimated gas injector to reduce the angular spread of the gas along B. The parallel extent of the GPI cloud could be measured using a separate camera viewing the cloud perpendicular to B. Off-line measurements of the density distribution in the gas cloud could verify its uniformity on the space and time scales of the turbulence. The GPI gas puff could contain a mixture of deuterium and helium to allow simultaneous 2-D imaging in several spectral lines to help distinguish the effects of electron density and temperature fluctuations.

Multiple GPI views at several points along the same B field line might be used to measure the parallel structure of edge turbulence, e.g., to look for ballooning effects at the outer midplane or possible blob variations along B. Remote optical control of viewing angle and zoom in GPI optics would allow searches for a smaller-scale (higher-k) structure in various poloidal and radial regions. Simultaneous views of the GPI gas cloud parallel and perpendicular to B should allow measurements of the pitch angle of the magnetic field lines as a function of radius by tracking individual filaments in both views, assuming the filaments lie along B. Imaging ion lines from impurity gas puffs such as methane or neon could be tried, even though ion filaments will extend along the B field line.

It would be interesting to have an *in situ* calibration the GPI response to electron density and temperature fluctuations using well-understood plasma waves or other diagnostics on the same B field line. Perhaps the radial oscillations due to low frequency MHD modes (or from externally imposed plasma jogs) can be used to calibrate GPI response, assuming the edge profiles shift rigidly with these motions. Other diagnostics such as correlation ECE emission, microwave reflectometry, or high resolution Thomson scattering could supplement the cross-checks of edge turbulence discussed in Sec. IV although these diagnostics are generally difficult in the plasma edge and SOL.

Improved modeling of the GPI diagnostic could be done using coupled 3-D neutral and magnetic field codes to calculate the expected 2-D spatial resolution over the entire image. Simulation of the shadowing effects of turbulence on the neutral cloud could be extended beyond the results discussed in Sec. V E using a variety of assumed perturbations and background plasma conditions, or input from turbulence simulations. The effects of the neutral gas cloud on plasma parameters could be better calculated using edge transport models such as UEDGE even without specific turbulence simulations.

The most important and most challenging direction for GPI is to validate and/or improve modeling of edge plasma turbulence in order to predict the performance of fusion devices. This can be done using improved synthetic diagnostics within these codes, allowing direct comparisons with GPI data. It is also important to continue to cross-check GPI results with other edge turbulence diagnostics such as BES, reflectometry, and probes, each of which has its own strengths and weaknesses.

SUPPLEMENTARY MATERIAL

See supplementary material for tables of the data shown in Figs. 6 and 7.

ACKNOWLEDGMENTS

[1]P. C. Liewer, Nucl. Fusion **25**, 543 (1985).
[2]S. J. Zweben, J. A. Boedo, O. Grulke, C. Hidalgo, B. LaBombard, R. J. Maqueda, P. Scarin, and J. L. Terry, Plasma Phys. Controlled Fusion **49**, S1 (2007).
[3]F. D. Halpern, J. L. Terry, S. J. Zweben, B. LaBombard, M. Podesta, and P. Ricci, Plasma Phys. Controlled Fusion **57**, 054005 (2015).
[4]*Methods of Experimental Physics*, edited by H. R. Griem and R. H. Lovberg (Academic Press, 1970), Vol. 9A, Chap. 10.
[5]D. H. J. Goodall, J. Nucl. Mater. **111-112**, 11 (1982).
[6]H. Niedermeyer, private communication (1982), this movie and GPI movies can be found at http://w3.pppl.gov/~szweben.
[7]C. M. Surko and R. E. Slusher, Science **221**, 817 (1983).
[8]S. J. Zweben, J. McChesney, and R. W. Gould, Nucl. Fusion **23**, 825 (1983).
[9]S. J. Zweben and S. S. Medley, Phys. Fluids B **1**, 2058 (1989).
[10]M. Endler, L. Giannone, K. McCormick, H. Niedermeyer, A. Rudyj, G. Theimer, N. Tsois, S. Zoletnik, and W7-AS Team, Phys. Scr. **51**, 610 (1995).
[11]M. Endler, H. Hiedermeyer, L. Giannone, E. Holzhauer, A. Rudyj, G. Theimer, N. Tsois, and ASDEX Team, Nucl. Fusion **35**, 1307 (1995).
[12]R. J. Maqueda, G. A. Wurden, S. J. Zweben, L. Roquemore, H. Kugel, D. Johnson, S. Kaye, S. Sabbagh, and R. Maingi, Rev. Sci. Instrum. **72**, 931 (2001).
[13]R. J. Maqueda, G. A. Wurden, D. P. Stotler, S. J. Zweben, B. LaBombard, J. L. Terry, J. L. Lowrance, V. J. Mastrocola, G. F. Renda, D. A. D'Ippolito, J. R. Myra, and N. Nishino, Rev. Sci. Instrum. **74**, 2020 (2003).
[14]S. J. Zweben, J. L. Terry, B. LaBombard, M. Greenwald, M. Muterspaugh, C. S. Pitcher, K. Hallatschek, R. J. Maqueda, B. Rogers, J. L. Lowrance, V. J. Mastrocola, and G. F. Renda, Phys. Plasmas **9**, 1981 (2002).
[15]J. L. Terry, R. Maqueda, C. S. Pitcher, S. J. Zweben, B. LaBombard, E. S. Marmar, A. Yu. Pigarov, and G. Wurden, J. Nucl. Mater. **290-293**, 757 (2001).
[16]J. L. Terry, S. J. Zweben, K. Hallatschek, B. LaBombard, R. J. Maqueda, B. Bai, C. J. Boswell, M. Greenwald, D. Kopon, W. M. Nevins, C. S. Pitcher, B. N. Rogers, D. P. Stotler, and X. Q. Xu, Phys. Plasmas **10**, 1739 (2003).
[17]D. P. Stotler, B. LaBombard, J. L. Terry, and S. J. Zweben, J. Nucl. Mater. **313-316**, 1066 (2003).

[18]C. C. Chaston, C. Salem, J. W. Bonnell, C. W. Carlson, R. E. Ergun, R. J. Strangeway, and J. P. McFadden, Phys. Rev. Lett. **100**, 175003 (2008).

[19]See http://sdo.gsfc.nasa.gov for images from the NASA Solar Dynamics Observatory.

[20]G. Y. Antar, J. H. Yu, and G. Tynan, Phys. Plasmas **14**, 022301 (2007).

[21]S. H. Muller, C. Theiler, A. Fasoli, I. Furno, B. Labit, G. R. Tynan, M. Xu, Z. Yan, and J. H. Yu, Plasma Phys. Controlled Fusion **51**, 055020 (2009).

[22]A. D. Light, S. C. Thakur, C. Brandt, Y. Sechrest, G. R. Tynan, and T. Munsat, Phys. Plasmas **20**, 082120 (2013).

[23]S. C. Thakur, C. Brandt, A. Light, L. Cui, J. J. Gosselin, and G. R. Tynan, Rev. Sci. Instrum. **85**, 11E813 (2014).

[24]C. Brandt, O. Grulke, T. Klinger, J. Negrete, Jr., G. Bousselin, F. Brochard, G. Bonhomme, and S. Oldenburger, Phys. Rev. E **84**, 056405 (2011).

[25]T. Carter, private communication (2016).

[26]D. Iraji, I. Furno, A. Fasoli, and C. Theiler, Phys. Plasmas **17**, 122304 (2010).

[27]A. Fasoli, A. Burckel, L. Federspiel, I. Furno, K. Gustafson, D. Iraji, B. Labit, J. Loizu, G. Plyushchev, P. Ricci, C. Theiler, A. Diallo, S. H. Mueller, M. Podestà, and F. Poli, Plasma Phys. Controlled Fusion **52**, 124020 (2010).

[28]S. Banerjee, H. Zushi, N. Nishino, K. Hanada, S. K. Sharma, H. Honma, S. Tashima, T. Tashima, T. Inoue, K. Nakamura, H. Idei, M. Hasegawa, and A. Fujisawa, Nucl. Fusion **52**, 123016 (2012).

[29]J. A. Alonso, S. J. Zweben, P. Carvalho, J. L. de Pablos, E. de la Cal, C. Hidalgo, T. Klinger, B. Ph. van Milligen, R. J. Maqueda, M. A. Pedrosa, C. Silva, M. Spolaore, H. Thomsen, and TJ-II Team, Plasma Phys. Controlled Fusion **48**, B465 (2006).

[30]D. Carralero, D. Carralero, E. de la Cal, J. L. de Pablos, A. de Coninck, J. A. Alonso, C. Hidalgo, B. Ph. van Milligen, and M. A. Pedrosa, J. Nucl. Mater. **390-391**, 457 (2009).

[31]G. Fuchert, G. Birkenmeier, B. Nold, M. Ramisch, and U. Stroth, Plasma Phys. Controlled Fusion **55**, 125002 (2013).

[32]G. Fuchert, G. Birkenmeier, M. Ramisch, and U. Stroth, Plasma Phys. Controlled Fusion **58**, 054005 (2016).

[33]B. D. Dudson, N. Ben Ayed, A. Kirk, H. R. Wilson, G. Counsell, X. Xu, M. Umansky, P. B. Snyder, B. Lloyd, and MAST Team, Plasma Phys. Controlled Fusion **50**, 124012 (2008).

[34]N. Ben Ayed, A. Kirk, B. Dudson, S. Tallents, R. G. L. Vann, H. R. Wilson, and MAST Team, Plasma Phys. Controlled Fusion **51**, 035016 (2009).

[35]S. Banerjee, H. Zushi, N. Nishino, K. Hanada, M. Ishiguro, S. Tashima, H. Q. Liu, K. Mishra, K. Nakamura, H. Idei, M. Hasegawa, A. Fujisawa, Y. Nagashima, and K. Matsuoka, Phys. Plasmas **21**, 072311 (2014).

[36]R. Pánek, J. Adámek, M. Aftanas, P. Bílková, P. Böhm, F. Brochard, P. Cahyna, J. Cavalier, R. Dejarnac, M. Dimitrova *et al.*, Plasma Phys. Controlled Fusion **58**, 104015 (2016).

[37]J. R. Harrison, G. M. Fishpool, A. J. Thornton, N. R. Walkden, and MAST Team, Phys. Plasmas **22**, 092508 (2015).

[38]J. L. Terry *et al.* "Fast imaging of filaments in the X-point region of Alcator C-Mod," Nucl. Mater. Energy (published online, 2017).

[39]R. J. Maqueda, D. P. Stotler, and NSTX Team, Nucl. Fusion **50**, 075002 (2010).

[40]S. Ku, R. Hager, C. S. Chang, J. M. Kwon, and S. E. Parker, J. Comp. Phys. **315**, 467 (2016).

[41]S. Ku, C. S. Chang, and P. H. Diamond, Nucl. Fusion **49**, 115021 (2009).

[42]G. McKee, R. Ashley, R. Durst, R. Fonck, M. Jakubowski, K. Tritz, K. Burrell, C. Greenfield, and J. Robinson, Rev. Sci. Instrum. **70**, 913 (1999).

[43]E. L. Foley and F. M. Levinton, Rev. Sci. Instrum. **84**, 043110 (2013).

[44]S. J. Zweben, R. J. Maqueda, R. Hager, K. Hallatschek, S. M. Kaye, T. Munsat, F. M. Poli, A. L. Roquemore, Y. Sechrest, and D. P. Stotler, Phys. Plasmas **17**, 102502 (2010).

[45]J. L. Terry, S. J. Zweben, M. V. Umansky, I. Cziegler, O. Grulke, B. LaBombard, and D. P. Stotler, J. Nucl. Mater. **390-391**, 339 (2009).

[46]I. Shesterikov, Y. Xu, M. Berte, P. Dumortier, M. Van Schoor, M. Vergote, B. Schweer, and G. Van Oost, Rev. Sci. Instrum. **84**, 053501 (2013).

[47]G. Fuchert *et al.*, Plasma Phys. Controlled Fusion **56**, 125001 (2014).

[48]D. D'Ippolito, J. R. Myra, and S. J. Zweben, Phys. Plasmas **18**, 065501 (2011).

[49]"Special issue on edge plasmas in magnetic fusion devices," Plasma Phys. Controlled Fusion **58** (2016), available at http://iopscience.iop.org/journal/0741-3335/page/Edge-plasmas-in-magnetic-fusion-devices.

[50]J. Terry, N. P. Basse, I. Cziegler, M. Greenwald, O. Grulke, B. LaBombard, S. J. Zweben, E. M. Edlund, J. W. Hughes, L. Lin, Y. Lin, M. Porkolab, M. Sampsell, B. Veto, and S. J. Wukitch, Nucl. Fusion **45**, 1321 (2005).

[51]H. Q. Wang, G. S. Xu, B. N. Wan, S. Y. Ding, H. Y. Guo, L. M. Shao, S. C. Liu, X. Q. Xu, E. Wang, N. Yan *et al.*, Phys. Rev. Lett. **112**, 185004 (2014).

[52]S. Banerjee, A. Diallo, and S. J. Zweben, Phys. Plasmas **23**, 044502 (2016).

[53]R. Maqueda, R. Maingi, and NSTX Team, Phys. Plasmas **16**, 056117 (2009).

[54]Y. Sechrest, T. Munsat, D. A. D'Ippolito, R. J. Maqueda, J. R. Myra, D. Russell, and S. J. Zweben, Phys. Plasmas **18**, 012502 (2011).

[55]I. Cziegler, P. H. Diamond, N. Fedorczak, P. Manz, G. R. Tynan, M. Xu, R. M. Churchill, A. E. Hubbard, B. Lipschultz, J. M. Sierchio, J. L. Terry, and C. Theiler, Phys. Plasmas **20**, 055904 (2013).

[56]I. Czielger, G. R. Tynan, P. H. Diamond, A. E. Hubbard, J. W. Hughes, J. Irby, and J. L. Terry, Plasma Phys. Controlled Fusion **56**, 075013 (2014).

[57]I. Czielger, G. R. Tynan, P. H. Diamond, A. E. Hubbard, J. W. Hughes, J. Irby, J. L. Terry *et al.*, Nucl. Fusion **55**, 083007 (2015).

[58]S. J. Zweben, D. P. Stotler, R. E. Bell, W. M. Davis, S. M. Kaye, B. P. LeBlanc, R. J. Maqueda, E. T. Meier, T. Munsat, Y. Ren, S. A. Sabbagh, Y. Sechrest, D. R. Smith, and V. Soukhanovskii, Plasma Phys. Controlled Fusion **56**, 095010 (2014).

[59]M. Agostini, P. Scarin, R. Cavazzana, L. Carraro, L. Grando, C. Taliercio, L. Franchin, and A. Tiso, Rev. Sci. Instrum. **86**, 123513 (2015).

[60]E. de la Cal, J. Guasp, and TJ-II Team, Plasma Phys. Controlled Fusion **53**, 085006 (2011).

[61]S. Gangadhara and B. LaBombard, Plasma Phys. Controlled Fusion **46**, 1617 (2004).

[62]S. J. Zweben, B. D. Scott, J. L. Terry, B. LaBombard, J. W. Hughes, and D. P. Stotler, Phys. Plasmas **16**, 082505 (2009).

[63]D. R. Bates, A. E. Kingston, and R. W. P. McWhirter, Proc. R. Soc. A **267**, 297 (1962).

[64]D. P. Stotler, D. A. D'Ippolito, B. LeBlanc, R. J. Maqueda, J. R. Myra, S. A. Sabbagh, and S. J. Zweben, Contrib. Plasma Phys. **44**, 294 (2004).

[65]D. P. Stotler, J. Boedo, B. LeBlanc, R. J. Maqueda, and S. J. Zweben, J. Nucl. Mater. **363-265**, 686 (2007).

[66]J. M. Muñoz Burgos, T. Barbui, O. Schmitz, D. Stutman, and K. Tritz, Rev. Sci. Instrum. **87**, 11E502 (2016).

[67]J. C. Weisheit, J. Phys. B **8**, 2556 (1975).

[68]R. K. Janev and J. J. Smith, At. Plasma-Mater. Interact. Data Fusion **4**, 1 (1993), supplement to the journal Nucl. Fusion, availalbe at http://www-pub.iaea.org/books/IAEABooks/1839/Atomic-and-Plasma-material-Interaction-Data-for-Fusion.

[69]I. Bray and A. T. Stelbovics, Phys. Rev. A **46**, 6995 (1992).

[70]I. Bray, D. V. Fursa, A. S. Kadyrov, A. T. Stelbovics, A. S. Kheifets, and A. M. Mukhamedzhanov, Phys. Rep. **520**, 135 (2012).

[71]M. Goto, J. Quant. Spectrosc. Radiat. Transfer **76**, 331 (2003).

[72]T. Fujimoto, J. Quant. Spectrosc. Radiat. Transfer **21**, 439 (1979).

[73]D. P. Stotler, F. Scotti, R. E. Bell, A. Diallo, B. P. LeBlanc, M. Podestà, A. L. Roquemore, and P. W. Ross, Phys. Plasmas **22**, 082506 (2015).

[74]B. Farizon, M. Barizon, M. J. Gaillard, E. Gerlic, and S. Ouaskit, Nucl. Instrum. Methods Phys. Res., Sect. B **101**, 287 (1995).

[75]D. Dunai, S. Zoletnik, J. Sárközi, and A. R. Field, Rev. Sci. Instrum. **81**, 103503 (2010).

[76]R. Cavazzana, P. Scarin, G. Serianni, M. Agostini, F. Degli Agostini, V. Cervaro, L. Lotto, Y. Yagi, H. Sakakita, H. Koguchi, and Y. Hirano, Rev. Sci. Instrum. **75**, 4152 (2004).

[77]M. Agostini, R. Cavazzana, P. Scarin, and G. Serianni, Rev. Sci. Instrum. **77**, 10E513 (2006).

[78]A. E. White, S. J. Zweben, M. J. Burin, T. A. Carter, T. S. Hahm, J. A. Krommes, and R. J. Maqueda, Phys. Plasmas **13**, 072301 (2006).

[79]G. Serianni, M. Agostini, R. Cavazzana, and P. Scarin, Plasma Phys. Controlled Fusion **49**, 2075 (2007).

[80]B. Cao, D. P. Stotler, S. J. Zweben, M. Bell, A. Diallo, and B. LeBlanc, Fusion Sci. Technol. **64**, 29 (2013), and references therein, available at http://www.ans.org/pubs/journals/fst/a_17044.

[81]*Nuclear Fusion Research, Understanding Plasma-surface Interactions*, edited by R. E. H. Clark and D. H. Reiter (Springer-Verlag Berlin Heidelberg, 2005).

[82]K. Behringer, H. P. Summers, B. Denne, M. Forrest, and M. Stamp, Plasma Phys. Controlled Fusion **31**, 2059 (1989).

83D. P. Stotler and C. F. F. Karney, Contrib. Plasma Phys. **34**, 392 (1994).

84O. Grulke, J. L. Terry, I. Cziegler, B. LaBombard, and O. E. Garcia, Nucl. Fusion **54**, 043012 (2014).

85S. J. Zweben, J. L. Terry, M. Agostini, W. M. Davis, A. Diallo, R. A. Ellis, T. Golfinopoulos, O. Grulke, J. W. Hughes, B. LaBombard, M. Landreman, J. R. Myra, D. C. Pace, and D. P. Stotler, Phys. Plasmas **20**, 072503 (2013).

86G. Birkenmeier, F. M. Laggner, M. Willensdorfer, T. Kobayashi, P. Manz, E. Wolfrum, D. Carralero, R. Fischer, B. Sieglin, G. Fuchert, U. Stroth, and ASDEX Upgrade Team, Plasma Phys. Controlled Fusion **56**, 075019 (2014).

87S. C. Liu, L. M. Shao, S. J. Zweben, G. S. Xu, H. Y. Guo, B. Cao, H. Q. Wang, L. Wang, N. Yan, S. B. Xia *et al.*, Rev. Sci. Instrum. **83**, 123506 (2012).

88G. S. Xu, L. M. Shao, S. C. Liu, H. Q. Wang, B. N. Wan, H. Y. Guo, P. H. Diamond, G. R. Tynan, M. Xu, S. J. Zweben *et al.*, Nucl. Fusion **54**, 013007 (2014).

89L. M. Shao, G. S. Xu, S. C. Liu, S. J. Zweben, B. N. Wan, H. Y. Guo, A. D. Liu, R. Chen, B. Cao, W. Zhang *et al.*, Plasma Phys. Controlled Fusion **55**, 105006 (2013).

90N. Nishino, L. Zang, M. Takeuchi, T. Mizuuchi, S. Ohshima, K. Kasajima, M. Sha, K. Mukai, H. Y. Lee, K. Nagasaki, H. Okada, T. Minami, S. Kobayashi, S. Yamamoto, S. Konoshima, Y. Nakamura, and F. Sano, J. Nucl. Mater. **438**, S540 (2013).

91L. Zang, T. Mizuuchi, N. Nishino, S. Ohshima, S. Yamamoto, Y. C. Sun, K. Kasajima, M. Takeuchi, K. Mukai, H. Y. Lee, N. Kenimochi, Y. Ohtani, K. Nagasaki, S. Kado, H. Okada, T. Minami, S. Kobayashi, N. Shi, S. Konoshima, Y. Nakamura, and F. Sano, Fusion Sci. Technol. **68**, 768 (2015).

92N. Nishino, Y. Nakashima, Y. Higashizono, S. Kobayashi, K. M. Islam, Y. Kubota, M. Yoshikawa, Y. Mishima, and T. Cho, Plasma Fusion Res.: Rapid Commun. **1**, 36 (2006), available at https://www.jstage.jst.go.jp/article/pfr/1/0/1_0_035/_article.

93Y. Nakashina, N. Nishino, Y. Higashizono, H. Kawano, S. Kobayashi, M. Shoji, Y. Kubota, M. Yoshikawa, M. K. Islam, Y. Mishima, D. Mimura, and T. Cho, J. Nucl. Mater. **363**, 616 (2007).

94S. J. Zweben, R. J. Maqueda, D. P. Stotler, A. Keesee, J. Boedo, C. E. Bush, S. M. Kaye, B. LeBlanc, J. L. Lowrance, V. J. Mastrocola, R. Maingi, N. Nishino, G. Renda, D. W. Swain, J. B. Wilgen, and NSTX Team, Nucl. Fusion **44**, 134 (2004).

95M. Agostini, P. Scarin, R. Cavazzana, F. Sattin, G. Serianni, M. Spolaore, and N. Vianello, Plasma Phys. Controlled Fusion **51**, 105003 (2009).

96P. Scarin, M. Agostini, R. Cavazzana, F. Sattin, G. Serianni, M. Spolaore, and N. Vianello, J. Nucl. Mater. **390-391**, 444 (2009).

97P. Scarin, M. Agostini, R. Cavazzana, F. Sattin, G. Serianni, and N. Vianello, J. Nucl. Mater. **363-365**, 669 (2007).

98M. Agostini, P. Scarin, G. Spizzo, N. Vianello, and L. Carraro, Plasma Phys. Controlled Fusion **56**, 095016 (2014).

99I. Shesterikov, Y. Xu, C. Hidalgo, M. Berte, P. Dumortier, M. Van Schoor, M. Vergote, G. Van Oost, and TEXTOR Team, Nucl. Fusion **52**, 042004 (2012).

100I. Shesterikov, Y. Xu, G. R. Tynan, P. H. Diamond, S. Jachmich, P. Dumortier, M. Vergote, M. Van Schoor, G. Van Oost, and TEXTOR Team, Phys. Rev. Lett. **111**, 055006 (2013).

101E. de la Cal, P. Semwal, A. Martın Aguilera, B. van Milligen, J. L. de Pablos, Z. Khan and C. Hidalgo, Plasma Phys. Controlled Fusion **56**, 105003 (2014).

102M. Agostini, R. Cavazzana, P. Scarin, G. Serianni, Y. Yagi, H. Koguchi, S. Kiyama, H. Sakakita, and Y. Hirano, Plasma Phys. Controlled Fusion **50**, 095004 (2008).

103R. Cavazzana, P. Scarin, G. Serianni, M. Agostini, F. Degli Agostini, V. Cervaro, L. Lotto, Y. Yagi, H. Sakakita, H. Koguchi, and Y. Hirano, Plasma Phys. Controlled Fusion **49**, 129 (2007).

104D. A. Russell, J. R. Myra, D. A. D'Ippolito, T. L. Munsat, Y. Sechrest, R. J. Maqueda, D. P. Stotler, S. J. Zweben, and NSTX Team, Phys. Plasmas **18**, 022306 (2011).

105J. Horacek, J. Horacek, J. Adamek, H. W. Muller, J. Seidl, A. H. Nielsen, V. Rohde, F. Mehlmann, C. Ionita, E. Havlıckova, and ASDEX Upgrade Team, Nucl. Fusion **50**, 105001 (2010).

106B. Nold, T. Ribeiro, M. Ramisch, Z. Huang, H. W. Muller, B. D. Scott, U. Stroth, and ASDEX Upgrade Team, New J. Phys. **14**, 063022 (2012).

107B. LaBombard, T. Golfinopoulos, J. L. Terry, D. Brunner, E. Davis, M. Greenwald, J. W. Hughes, and Alcator C-Mod Team, Phys. Plasmas **21**, 056108 (2014).

108J. A. Boedo, J. R. Myra, S. Zweben, R. Maingi, R. J. Maqueda, V. A. Soukhanovskii, J. W. Ahn, J. Canik, N. Crocker, D. A. D'Ippolito, R. Bell, H. Kugel, B. Leblanc, L. A. Roquemore, D. L. Rudakov, and NSTX Team, Phys. Plasmas **21**, 042309 (2014).

109A. L. Roquemore, S. J. Zweben, R. Kaita, R. J. Marsalsa, C. E. Bush, and R. J. Maqueda, Rev. Sci. Instrum. **79**, 10F124 (2008).

110M. Willensdorfer, G. Birkenmeier, R. Fischer, F. M Laggner, E. Wolfrum, G. Veres, F. Aumayr, D. Carralero, L. Guimarais, B. Kurzan, and ASDEX Upgrade Team, Plasma Phys. Controlled Fusion **56**, 025008 (2014).

111R. J. Fonck, P. A. Duperrex, and S. F. Paul, Rev. Sci. Instrum. **61**, 3487 (1990).

112G. McKee, R. J. Fonck, M. W. Shafer, I. U. Uzun-Kaymak, and Z. Yan, Rev. Sci. Instrum. **81**, 10D741 (2010).

113D. R. Smith, R. J. Fonck, G. R. McKee, D. S. Thompson, R. E. Bell, A. Diallo, W. Guttenfelder, S. M. Kaye, B. P. LeBlanc, and M. Podesta, Nucl. Fusion **53**, 113029 (2013).

114A. R. Field, D. Dunai, Y. C. Ghim, P. Hill, B. McMillan, C. M. Roach, S. Saarelma, A. A. Schekochihin, S. Zoletnik, and MAST Team, Plasma Phys. Controlled Fusion **56**, 025012 (2014).

115S. Zoletnik, M. Anton, M. Endler, S. Fiedler, M. Hirsch, K. McCormick, J. Schweinzer, and the W7-AS Team, Phys. Plasmas **6**, 4239 (1999).

116Y. Sechrest, D. Smith, D. P. Stotler, T. Munsat, and S. J. Zweben, Phys. Plasmas **22**, 052310 (2015).

117D. A. Russell, J. R. Myra, D. A. D'Ippolito, B. LaBombard, J. W. Hughes, J. L. Terry, and S. J. Zweben, Phys. Plasmas **23**, 062305 (2016).

118C. Theiler, J. L. Terry, E. Edlund, I. Cziegler, R. M. Churchill, J. W. Hughes, B. LaBombard, T. Golfinopoulos, and Alcator C-Mod Team, Plasma Phys. Controlled Fusion **59**, 025016 (2017).

119P. W. Wachulak, Rev. Sci. Instrum. **87**, 091501 (2016) and references therein.

120B. Landgraf, M. Schnell, A. Sävert, M. C. Kaluza, and C. Spielmann, Rev. Sci. Instrum. **82**, 083106 (2011).

121V. Malka, C. Coulaud, J. P. Geindre, V. Lopez, Z. Najmudin, D. Neely, and F. Amiranoff, Rev. Sci. Instrum. **71**, 2329 (2000).

122D. Moulton, Y. Marandet, P. Tamain, Ph. Ghendrih, and M. Groth, J. Nucl. Mater. **463**, 893 (2015).

123D. Moulton, Y. Marandet, P. Tamain, Ph. Ghendrih, and R. Futtersack, Contrib. Plasma Phys. **54**, 575 (2014).

124J. R. Myra, D. A. Russell, D. A. D'Ippolito, J.-W. Ahn, R. Maingi, R. J. Maqueda, D. P. Lundberg, D. P. Stotler, S. J. Zweben, J. Boedo, M. Umansky, and NSTX Team, Phys. Plasmas **18**, 012305 (2011).

125R. K. Janev, W. D. Langer, K. Evans, Jr., and D. E. Post, Jr., *Elementary Processes in Hydrogen-helium Plasmas*, Springer Series on Atoms and Plasmas (Springer-Verlag, New York, 1987).

126S. Brezinsek, Ph. Mertens, A. Pospieszczyk, G. Sergienko, and P. T. Greenland, Contrib. Plasma Phys. **42**, 668 (2002).

127U. Fantz, D. Reiter, B. Heger, and D. Coster, J. Nucl. Mater. **290-293**, 367 (2001).

128S. Menmuir, E. Rachlewa, U. Fantz, R. Pugnoc, R. Duxc, and ASDEX Upgrade Team, J. Quant. Spectrosc. Radiat. Transfer **105**, 425 (2007).

129V. Kotov, D. Reiter, R. A. Pitts, S. Jachmich, A. Huber, D. P. Coster, and JET-EFDA Contributors, Plasma Phys. Controlled Fusion **50**, 105012 (2008).

130K. Behringer and U. Fantz, New J. Phys. **2**, 23 (2000).

131B. Heger, U. Fantz, K. Behringer, and the ASDEX Upgrade Team, J. Nucl. Mater. **290-293**, 413 (2001).

132P. T. Greenland, Proc. R. Soc. A **457**, 1821 (2001).

133A. Pigarov and S. Krasheninnikov, Phys. Lett. A **222**, 251 (1996).

134R. K. Janev, D. Reiter, and U. Samm, Forschungszentrum Juelich Report Juel-4105, 2003.

135P. T. Greenland and D. Reiter, Contrib. Plasma Phys. **38**, 302 (1998).

136S. Ma, J. Howard, and N. Thapar, Phys. Plasmas **18**, 083301 (2011).

137S. I. Krasheninnikov and A. Yu. Pigarov, in *Proceedings of the 11th International Conference on Plasma Physics and Controlled Fusion Research (Kyoto, November 1986)*, paper IAEA-CN-47/H-III-10 (IAEA, Vienna, 1987), Vol. 3, p. 387.

138R. Marchand and J. Lauzon, Phys. Fluids B **4**, 924 (1992).

139A. S. Wan, H. E. Dalhed, H. A. Scott, D. E. Post, and T. D. Rognlien, J. Nucl. Mater. **220-222**, 1102 (1995).

140J. L. Terry, B. Lipschultz, A. Yu. Pigarov, S. I. Krasheninnikov, B. LaBombard, D. Lumma, H. Ohkawa, D. Pappas, and M. Umansky, Phys. Plasmas **5**, 1759 (1998).

[141]M. L. Adams, H. A. Scott, R. W. Leeb, J. L. Terry, E. S. Marmar, B. Lipschultz, A. Yu. Pigarov, and J. P. Freidberga, J. Quant. Spectrosc. Radiat. Transfer **71**, 117 (2001).

[142]D. Reiter, S. Wiesen, and M. Born, Plasma Phys. Controlled Fusion **44**, 1723 (2002).

[143]S. Sasaki, S. Takamura, S. Watanabe, S. Masuzaki, T. Kato, and K. Kadota, Rev. Sci. Instrum. **67**, 3521 (1996).

[144]Y. Iida, S. Kado, A. Otamoto, S. Kajita, T. Shikama, D. Yamasaki, and S. Tanaka, J. Plasma Fusion Res. Ser. **7**, 123 (2006).

[145]D. Nishijima and E. M. Hollmann, Plasma Phys. Controlled Fusion **49**, 791 (2007).

[146]S. Kajita, N. Ohno, S. Takamura, and T. Nakano, Phys. Plasmas **13**, 013301 (2006).

[147]S. Kajita, N. Ohno, S. Takamura, and T. Nakano, Phys. Plasmas **16**, 029901 (2009).

[148]F. B. Rosmej, N. Ohno, S. Takamura, and S. Kajita, Contrib. Plasma Phys. **48**, 243 (2008).

[149]J. M. Muñoz Burgos, M. Agostini, P. Scarin, D. P. Stotler, E. A. Unterberg, S. D. Loch, O. Schmitz, K. Tritz, and D. Stutman, Phys. Plasmas **23**, 053302 (2016).

[150]M. L. Adams and H. A. Scott, Contrib. Plasma Phys. **44**, 262 (2004).

[151]H. A. Scott and M. L. Adams, Contrib. Plasma Phys. **44**, 51 (2004).

[152]S. Kajita and N. Ohno, Rev. Sci. Instrum. **82**, 023501 (2011).

[153]T. A. Gianakon, R. J. Fonck, J. D. Callen, R. D. Durst, J. S. Kim, and S. F. Paul, Rev. Sci. Instrum. **63**, 4931 (1992).

[154]Y. Marandet, P. Tamain, R. Futtersack, Ph. Ghendrih, H. Bufferand, P. Genesio, and A. Mekkaoui, J. Nucl. Mater. **438**, S518 (2013).

[155]A. S. Thrysøe, L. E. H. Tophøj, V. Naulin, J. J. Rasmussen, J. Madsen, and A. H. Nielsen, Plasma Phys. Controlled Fusion **58**, 044010 (2016).

[156]A. Mekkaoui, Y. Marandet, D. Reiter, P. Boerner, P. Genesio, J. Rosato, H. Capes, M. Koubiti, L. Godbert-Mouret, and R. Stamm, Phys. Plasmas **19**, 122310 (2012).

[157]A. Mekkaoui, V. Kotov, D. Reiter, and P. Boerner, Contrib. Plasma Phys. **54**, 409 (2014).

[158]R. Jha, A. Sen, P. K. Kaw, P. K. Atrey, S. B. Bhatt, N. Bisai, K. Tahiliani, R. L. Tanna, and ADITYA Team, Plasma Phys. Controlled Fusion **51**, 095010 (2009).

[159]D. Sangwan, R. Jha, J. Brotankova, and M. V. Gopalkrishna, Phys. Plasmas **20**, 062503 (2013).

[160]I. Cziegler, J. L. Terry, J. W. Hughes, and B. LaBombard, Phys. Plasmas **17**, 056120 (2010).

[161]S. J. Zweben, S. J. Zweben, W. M. Davis, S. M. Kaye, J. R. Myra, R. E. Bell, B. P. LeBlanc, R. J. Maqueda, T. Munsat, S. A. Sabbagh, Y. Sechrest, D. P. Stotler, and NSTX Team, Nucl. Fusion **55**, 093035 (2015).

[162]B. A. Carreras, L. W. Owen, R. Maingi, and P. K. Mioduszewski, T. N. Carlstrom, and R. J. Groebner, Phys. Plasmas **5**, 2623 (1998).

[163]J. Omotani, I. Pusztai, S. Newton, and T. Fülöp, Nucl. Fusion **56**, 124002 (2016).

[164]N. Bisai and P. W. Kaw, Phys. Plasmas **23**, 092509 (2016).

[165]T. Munsat and S. J. Zweben, Rev. Sci. Instrum. **77**, 103501 (2006).

[166]S. Banerjee, H. Zushi, N. Nishino, K. Mishra, T. Onchi, A. Kuzmin, Y. Nagashima, K. Hanada, K. Nakamura, H. Idei, M. Hasegawa, and A. Fujisawa, Rev. Sci. Instrum. **86**, 033505 (2015).

[167]J. M. Sierchio, I. Cziegler, J. L. Terry, A. E. White, and S. J. Zweben, Rev. Sci. Instrum. **87**, 023502 (2016).

[168]I. Cziegler, J. L. Terry, S. J. Wukitch, M. L. Garrett, C. Lau, and Y. Lin, Plasma Phys. Controlled Fusion **54**, 015019 (2012).

[169]D. Pugmire, private communication (2016).